Spectral theory for nonlinear superconducting microwave systems: Extracting relaxation rates and mode hybridization

Dung N. Pham,[1,*] Richard D. Li,[2] and Hakan E. Türeci[1]

[1] *Department of Electrical and Computer Engineering, Princeton University, Princeton, New Jersey 08544, USA*
[2] *Department of Physics, Yale University, New Haven, Connecticut 06511, USA*

(Received 11 November 2023; revised 9 April 2024; accepted 15 May 2025; published 4 June 2025)

The accurate modeling of mode hybridization and calculation of radiative relaxation rates have been crucial to the design and optimization of superconducting quantum devices. In this work, we introduce a spectral theory for the electrohydrodynamics of superconductors that enables the extraction of the relaxation rates of excitations in a general three-dimensional distribution of superconducting bodies. Our approach addresses the long-standing problem of formulating a modal description of open systems that is both efficient and allows second quantization of the radiative hybridized fields. This is achieved through the implementation of finite but transparent boundaries through which radiation can propagate into and out of the computational domain. The resulting spectral problem is defined within a coarse-grained formulation of the electrohydrodynamical equations that is suitable for the analysis of the nonequilibrium dynamics of multiscale superconducting quantum systems.

DOI: 10.1103/slwj-33nx

I. INTRODUCTION

Engineered superconducting systems used in analog quantum simulation [1,2], quantum sensing [3,4], and quantum computing [5,6] are described by the electrohydrodynamic theory of superconducting systems, first proposed without justification by Feynman [7] in a special lecture he delivered in the 1960s. Few attempts have been made to either justify [8,9] or solve [10] this model's equations of motion exactly, but simplified versions [11–13] have been considered via various modifications to minimal coupling. This low-energy theory can be credited as the underpinning of Josephson phenomena, flux quantization, and, generally, the physics of vortices. The second-quantized version of it constitutes the basis of the formulation known as circuit quantum electrodynamics (QED) [14], which has been the workhorse behind the current understanding of the physics governing superconducting quantum computers. As systems grow increasingly sophisticated and their electromagnetic (EM) environments become more complex, efficient computational strategies in both the classical regime and the quantum regime are much needed to produce accurate reduced models containing the degrees of freedom of interest. This has given rise to an active research area at the intersection of computational electromagnetism, circuit theory, and quantum electrodynamics of superconducting devices [15–24] to analyze and model the physics of these circuits.

An indispensable component in the electrodynamic modeling of superconducting circuits is the extraction of relaxation rates. Purcell modification of radiative lifetimes of qubits is today an essential mechanism for the protection of qubits and plays an important role in the electromagnetic design of the entire processor [25–28]. Additionally, in applications that require strong rf or microwave excitations of individual oscillators, new dissipative processes and interlevel transitions can be activated [29–37]. These processes, in turn, depend strongly on the spectral characteristics of the electromagnetic environment in which the nonlinear elements are embedded [33]. Resource-intensive numerical simulations are needed to extract such information for complex quantum-electrodynamic systems. Such simulations are not only computationally demanding but also face conceptual difficulties arising from the infinite degrees of freedom inherent in QED [38]. These conceptual issues as they appear in superconducting quantum devices [25,39] require careful analysis of the system to avoid unphysical divergences [40–45]. The divergence issues can be resolved effectively by one choosing the correct set of modes to expand as in Refs. [43,44]. In the language of lumped-element circuits, this means the modes have to incorporate the details in the couplings between circuit elements [18,46] (e.g., the exact position of the qubits in the resonators, and the coupling capacitances). From the electromagnetic point of view, this boils down to one properly handling hybridization between the modes of subcomponents in the system (e.g., qubit modes and cavity modes in a minimal quibit-cavity sytem), while respecting

*Contact author: dnpham@princeton.edu

gauge invariance. Therefore, in principle, an approach to modeling that is based on a rigorous spectral theory allows the accurate quantification of limitations brought about by noise [47–49], dissipation [50,51], and undesired interactions [52,53] within the system and its electromagnetic environment.

In the present work, we introduce a spectral theory of electrohydrodynamics of superconductors (EHDS) from which the relaxation rates of general three-dimensional (3D) superconducting circuits can be obtained. This spectral theory is adapted to a coarse-grained description of the EHDS equations, known as DEC-QED, previously derived and analyzed in Ref. [10]. DEC-QED provides the following advantages: (1) Through its structure-preserving geometric discretization procedure, known as discrete exterior calculus (DEC), this formulation enables stable long-time simulations. (2) By virtue of the fundamental fields being hybridized gauge-invariant fields rather than the standard electromagnetic potentials, different materials can be handled in a uniform fashion. (3) At a superconductor–normal metal–superconductor junction, the hybridized field is identical to the gauge-invariant Josephson phase across the junction. (4) For transmission lines and lumped-element circuits and in the limit of a perfect superconductor ($\lambda_L = 0$), DEC-QED equations reduce to the standard circuit QED equations.

The difficulty with developing a spectral theory stems from the desire to solve the EHDS equations, a set of nonlinear partial differential equations (PDEs) describing the evolution of the order parameter of a charged fluid coupled to Maxwell's equations, in a finite spatial domain. Ideally, one would like to keep the computational domain as small as possible, just as large as the superconducting system itself. However, this is not possible, because we also need to keep the volume as large as possible to allow there to be radiative relaxation of the excitations in the superconductor. The optimal solution to avoid this trade-off is to use a modal description for a finite but open domain subject to transparent boundary conditions (BCs) for EM radiation. This allows us to keep the computational domain small enough to be computationally feasible, while still allowing the radiative relaxation of the excitations. While boundary conditions such as the perfectly matched layer [54,55] or absorbing boundary conditions [56,57] are known and very useful in classical EM problems, it is also desirable to implement a transparent boundary so that solving the corresponding spectral problem would provide a modal decomposition that can serve as the basis for second quantization of the EHDS equations. This, however, has been a difficult problem that remains unaddressed since the full formulation of quantum electrodynamics [58] because such boundary conditions result in non-Hermitian modes [59–61]. Recently, it was shown that by the use of the Heisenberg equations of motion for quantum field operators, this issue can be circumvented in the context of 1D transmission line systems through the use of singular function expansion and a suitable spectral problem [62]. Here we generalize the statement of this spectral problem to the solution of the nonlinear EHDS equations (the original spectral problem was defined [62] in the context of circuit QED, which assumes fields do not penetrate the superconductors), and to general three-dimensional domains. We do not address the issue of quantization, but focus on the spectral problem that arises through the linearization of the EHDS equations, the resulting non-Hermitian modes, and the calculation of dissipation rates for all modes. The dissipation rates for "qubitlike" modes are precisely their Purcell radiative lifetimes [63], while for the more spatially extended modes, they represent their losses due to their hybridization with radiative channels in the system [64–66].

With reference to the prior work on modeling of superconducting devices, our approach is within the class of full-wave methods [67,68]. With respect to existing full-wave methods for superconducting systems, DEC-QED has two important distinctions: (1) *Calculation of radiative losses.* The boundary conditions implemented in existing approaches to capture radiative losses are often absorbing boundary conditions. Most frequently, radiative losses at a 3D cavity's ports are modeled by adaptation of the lumped-element models and termination of the ports with 50 Ω matched resistors [69] or by the covering of the holes on the cavity walls with resistive disks [20]. Although this approach is effective in obtaining the frequencies of the eigenemodes, it is known to fail to accurately capture the spatial structure of the open modes. More importantly, no known method exists for second quantization using such modes, and therefore such EM full-wave simulations cannot rigorously be used to synthesize a quantum mechanical Hamiltonian or Liouvillian. Often the quantum Hamiltonian is derived from simulations ignoring radiative losses, and the relaxation rates are introduced through a perturbative approach. Previous efforts in improving the modeling of radiative losses due to coupling to transmission lines include solving the 1D wave equation in the transmission lines with boundary conditions imposed at the ends of the long waveguide [41,44,45] or implementation of outgoing radiation at a finite-range transparent boundary [18]. In this paper, we follow the latter approach and generalize it beyond (1 + 1)D models to arbitrarily shaped structures and physical layouts. DEC-QED builds on prior work in classical electromagnetic systems for the implementation of correct open (transparent) boundary conditions [70,71], which was recently shown to serve as a mathematically consistent basis for second quantization of the modes of a transmission line cavity [62]. (2) *Time-dependent evolution.* DEC-QED aims at numerically solving the set of nonlinear PDEs describing the electrohydrodynamics of the superconducting condensate coupled to fields described by Maxwell equations. This allows DEC-QED to describe

the evolution of gauge-invariant hybridized fields existing throughout free space and the superconductors, avoiding issues that arise in defining boundary conditions at superconductor/vacuum boundaries whose accuracy is not controlled. Compared with existing full-wave methods, this is a special feature of our approach. The linearized spectral solutions of DEC-QED then serve as a basis for expanding this nonlinear dynamics. In the current work, we do not discuss the nonlinear aspects of evolution, which are discussed at length in Ref. [10].

The main results presented in this paper are organized as follows: In Sec. II we discuss the electrohydrodynamic model used to describe the dynamics of the superconducting condensate coupled to the EM environment and derive the spectral problem to be solved. In Sec. III we briefly discuss the formulation of DEC-QED used in the rest of the article for coarse-grained calculations. Next, we demonstrate the convergence in the calculations for the spectral profile of a sample superconducting cavity. Simplicial and cubical meshing strategies are benchmarked in Sec. IV A. In Sec. IV B we show how mode hybridization due to accidental degeneracies can be encountered in the calculations of the modes for a symmetric cavity and that our method can distinguish the degenerate modes through the inclusion of a small perturbation of the cavity shape. In Sec. IV C we demonstrate coarse-grained calculations of hybridized modes for multiscale systems containing multiple components. Finally, we present two main approaches for implementing open boundary conditions based on (1) Green's boundary integrals in Secs. V A and V B and (2) vector spherical harmonics (VSH) expansions in Sec. V C, along with numerical examples, to demonstrate the accuracy and effectiveness of these methods. We have made the implementation of the formulation discussed here available as part of an open-source DEC-QED repository [72].

II. ELECTROHYDRODYNAMIC FORMULATION OF SUPERCONDUCTING MATERIALS

Consider a multiply connected region composed of different dielectric and superconducting materials. Well below the critical temperature, where most superconducting devices operate, the superconducting material can be modeled as a charged condensate [8,9] trapped by a background of positive charge ($\rho_{\rm src}$). The dynamics of the condensate are wholly determined through minimal coupling to the dynamical electromagnetic potentials ($\mathbf{A}$, V) and the Coulomb attraction to the static positive background (U) defining the superconductor. We refer to the resulting order parameter equation [7] and Maxwell's equations as the EHDS equations

$$i\hbar\frac{\partial\Psi(\mathbf{r},t)}{\partial t}=\left[\frac{1}{2m}(-i\hbar\nabla-q\mathbf{A})^2+qV(\mathbf{r},t)+U(\mathbf{r})\right]\Psi(\mathbf{r},t) \tag{1}$$

and Maxwell's equations

$$\nabla\times\nabla\times\mathbf{A}+\mu_0\epsilon\ddot{\mathbf{A}}=\mu_0(\mathbf{J}_s+\mathbf{J}_{\rm src})-\mu_0\epsilon\nabla\dot{V}, \tag{2}$$

$$\nabla^2V+\frac{\partial}{\partial t}(\nabla\cdot\mathbf{A})=-\frac{q}{\epsilon}(\rho+\rho_{\rm src}), \tag{3}$$

where ρ and $\mathbf{J}_s$ are the condensate density and the supercurrent, respectively, and $\rho_{\rm src}$ and $\mathbf{J}_{\rm src}$ are the external charge and the source current. Here $q=2e$ and $m=2m_e$ are the charge and mass of a Cooper pair, respectively, which are twice the charge e and mass m_e of an electron. Generally, we include the positive background defining the superconducting regions in $\rho_{\rm src}$. Dielectric regions are defined by $\epsilon(\mathbf{r})=\tilde{\epsilon}(\mathbf{r})\epsilon_0$, where $\tilde{\epsilon}$ is the stepwise constant relative permittivity function, which is unity when a dielectric is not present and is greater than 1 otherwise. Using the Madelung representation for the condensate wave function, $\Psi(\mathbf{r},t)=\sqrt{\rho(\mathbf{r},t)}e^{i\theta(\mathbf{r},t)}$, and introducing the gauge-invariant hybridized field $\boldsymbol{\mathcal{A}}=\mathbf{A}-(\hbar/q)\nabla\theta$, we can write Eqs. (1)–(3) in the forms [10]

$$\nabla\times\nabla\times\boldsymbol{\mathcal{A}}+\mu_0\epsilon\frac{\partial^2\boldsymbol{\mathcal{A}}}{\partial t^2}+\frac{\mu_0q^2}{m}\rho\boldsymbol{\mathcal{A}}-\frac{\mu_0\epsilon q}{2m}\frac{\partial}{\partial t}\nabla|\boldsymbol{\mathcal{A}}|^2+\frac{\mu_0\epsilon\hbar^2}{2mq}\frac{\partial}{\partial t}\nabla\left[\frac{\nabla^2(\sqrt{\rho})}{\sqrt{\rho}}\right]=\mu_0\mathbf{J}_{\rm src} \tag{4}$$

and

$$\frac{\partial\rho}{\partial t}=\nabla\cdot\left[\frac{q}{m}\rho\boldsymbol{\mathcal{A}}-\frac{\mathbf{J}_{\rm src}}{q}\right]-\frac{\partial\rho_{\rm src}}{\partial t}. \tag{5}$$

These equations were derived and the resulting real-time dynamics under specific conditions were analyzed in Ref. [10]. Here we are interested in the spectral problem associated with these nonlinear equations. Linearization can be done by one splitting the condensate density ρ into the mean value ρ_0 that exactly balances the positively charged ionic background and the fluctuation $\delta\rho$ arising from interactions with the external EM field. The linear sector of Eq. (4) that corresponds to the transverse excitations then reproduces London theory [73] and is sourced by the fluctuation in the source current. A derivation of the linearization is provided in Appendix A. The resulting inhomogeneous source-field equations can be solved through the spectral problem of a vector Helmholtz equation for the gauge-invariant hybridized field $\boldsymbol{\mathcal{A}}$:

$$\nabla\times\nabla\times\boldsymbol{\mathcal{A}}+\left(\frac{1}{\lambda_L^2(\mathbf{r})}-n^2(\mathbf{r})k^2\right)\boldsymbol{\mathcal{A}}=0, \tag{6}$$

where the distribution of superconducting and dielectric materials is given by the local London penetration depth function $\lambda_L(\mathbf{r})=\sqrt{m/\mu_0q^2\rho_0(\mathbf{r})}$ and the refractive index function $n(\mathbf{r})=\sqrt{\tilde{\epsilon}(\mathbf{r})}$, respectively, and k is

the wave number. By defining a spectral problem for hybridized fields that permeate the entire space, we can directly address mode hybridization, which comes from the inevitable hybridization of the electromagnetic environments of individual elements in the system such as qubits, resonators, the substrates, or packaging. Solving the eigenproblem in Eq. (6) with appropriate radiative boundary conditions produces a set of modes that carries all information on hybridization and on the radiative loss of the full system.

III. DEC-QED FORMULATION

DEC-QED provides a spatially-coarse-grained description of a physical system governed by nonlinear PDEs. The fundamental field variables are small integrals of the original microscopic continuous fields over finite spatial intervals. This results in a discretized model that is computationally efficient and still accurate within the resolution of a given measurement apparatus. In this section, we provide a minimal introduction to the geometric constructions in DEC that are needed for computing electromagnetic modes in systems that may contain an arbitrary distribution of superconducting and dielectric materials, all within a finite computational domain. For a more comprehensive discussion of the formulation, see Ref. [10].

In DEC, the discretization of PDEs requires a dual-mesh construction, within which the d-dimensional computational space is discretized by a *primal mesh* M that conforms to the boundaries of the enclosed physical domain and the interfaces between materials. The fundamental building blocks of the primal mesh can be simplices (i.e., triangles in two dimensions and tetrahedra in three dimensions) or cubical elements. The vertices of the *dual mesh* $M^\dagger$ are then circumcenters of the primal d-dimensional cells, and the edges of $M^\dagger$ are generated by one connecting the neighboring circumcenters. Throughout this paper, we use a dagger symbol to denote a dual quantity. For elements strictly inside the computational space, the mappings from vertices v, edges e, faces f , and cells c in M to cells $v^\dagger$, faces $e^\dagger$, edges $f^\dagger$, and vertices $c^\dagger$, respectively in $M^\dagger$ are one-to-one. This bijective correspondence is not applicable at the computational boundary, where the dual elements are truncated, which leads to auxiliary dual nodes lying on the boundary of M [see Figs. 1(a) and 1(b)]. During numerical calculations, this truncation of the dual mesh is taken care of by the appropriate application of boundary conditions.

In this DEC framework, scalar fields lie on either primal vertices v or their dual volume $v^\dagger$, while vectorial quantities are projected onto the discrete primal edges e or assigned to the dual faces $e^\dagger$. For example, given a vector field $\boldsymbol{\mathcal{A}}$, we construct the coarse-grained edge field

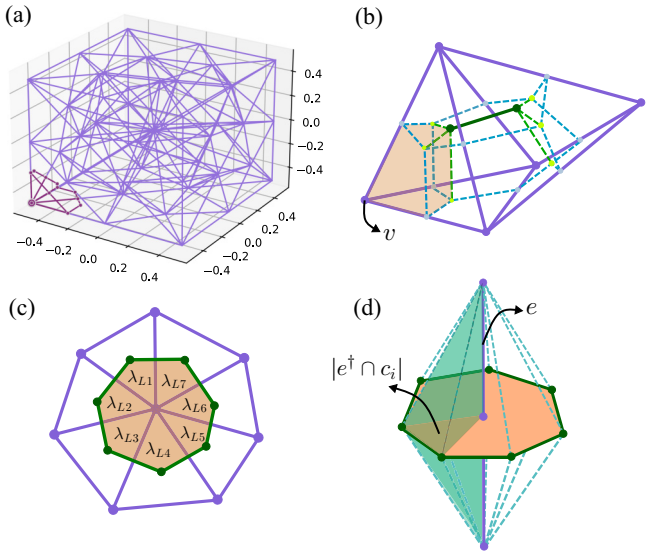

FIG. 1. (a) An example primal mesh. The highlighted edges in the lower-left corner form the boundary of an auxiliary dual volume. (b) Close-up view of a node v that lies on the boundary of the primal mesh. The neighboring dual nodes are shown in dark green, while the auxiliary boundary dual nodes are shown in bright green. The shaded volume is the truncated volume $v^\dagger$ dual to the node v. (c) 2D example of a vertex that lies at the interface among multiple material regions. The material properties assigned to this node are the weighted average of the values in the surrounding regions. (d) 3D example of an edge lying at a material interface composed of multiple cells c_i. The darkened triangle is the intersection of the dual face $e^\dagger$ with the cell c_i, and the shaded volume is the portion of the support volume of e that lies inside c_i.

$$\boldsymbol{\Phi}(e) = \int_e \mathbf{d}\ell \cdot \boldsymbol{\mathcal{A}}, \tag{7}$$

where the integration is done along the primal edge e, and given a scalar function ρ, we define the coarse-grained variable

$$Q(v^\dagger) = \int_{v^\dagger} dV\rho, \tag{8}$$

where the integration is done over the dual volume $v^\dagger$. By solving the equations governing these coarse-grained fields, we can probe the properties of the system.

To properly account for the distribution of different materials within the computational domain, material properties such as the dielectric function n^2 or $1/\lambda_L^2$ (which is proportional to the bulk condensate density) can be assigned to objects lying on the dual mesh. For example, for every edge e, a value for $1/\lambda_L^2$ is assigned to its dual $e^\dagger$. This procedure is particularly convenient if e lies at the interface between multiple materials. The dual $e^\dagger$ in such cases would intersect with all the different material domains that share this edge, and the effective value

$\overline{1/\lambda_L^2}(e^\dagger)$ there will be the weighted average of the values in the surrounding domains [see Fig. 1(d)]. In a three-dimensional setting, this is formally defined as followed: Let $\{c_i\}$ be the list of all the cells that share an edge e. Then

$$\overline{\left(\frac{1}{\lambda_L^2}\right)}(e^\dagger) = \sum_{c_i} \frac{|e^\dagger \cap c_i|}{\Delta A(e^\dagger)} \frac{1}{\lambda_L^2(c_i)}, \tag{9}$$

where $|e^\dagger \cap c_i|$ is the area of the intersection between $e^\dagger$ and c_i, and $\Delta A(e^\dagger)$ is the area of $e^\dagger$.

This DEC formulation of the electrohydrodynamics of coarse-grained quantities offers several benefits: (1) Since the gauge-invariant fields ($\mathcal{A}$, ρ) permeate all of space, the issues related to boundary conditions at material interfaces are simplified by the introduction of effective material properties. (2) In addition, because the Josephson phase is, by definition, precisely the field $\mathbf{\Phi}(e_J)$ evaluated at the edge e_J defined across the junction, our method is consistent with the standard description of Josephson dynamics. (3) Moreover, this approach provides a prescription to extend the formulation of electrodynamics with the use of gauge-invariant, coarse-grained flux variables to any arbitrary medium. Therefore, this is a rigorous generalization of the coarse-grained formulation beyond the junction and applies to the entire discretized 3D (2D) computational space. In this extension to the full 3D structure, the generalized flux variable $\mathbf{\Phi}$ lies on the edges of the mesh that discretizes the entire system, while the charge Q lies on the vertices. This approach is therefore a combination of flux-based and charge-based formulations, which has been shown to provide a more comprehensive description of superconducting circuits [22,24]. When we apply this description of the full 3D electromagnetic problem to the superconducting coplanar transmission line and restrict ourselves to only the quasi-1D description of the fluxes defined across the superconducting islands, the well-known dynamical equations governing the flux and charge variables are exactly reproduced without our having to evoke the lumped-element picture [10]. (4) Physical constraints such as the current-charge continuity and energy conservation are preserved by our coarse-grained formulation of the electromagnetic problem. Additional geometric constraints on vector fields are also satisfied exactly by our approach [10] as it is based on DEC—a structure-preserving theory of discrete spaces. Moreover, since our formulation of the EHDS problem deals exclusively with gauge-invariant variables, we do not need to impose any additional constraints on the gauge field.

Furthermore, because here the fundamental variables of interest are the coarse-grained fields that hybridize light and matter, this approach is fundamentally different from other full-wave methods. The quantization of this electromagnetic theory can be done in spirit similar to that for 1D transmission line circuit QED [64], but now with fluxes lying on the edges and charges lying on the nodes of the fully discretized 3D (2D) system. This approach, in which all of the classical and quantum analysis is done at the EM field level, is distinct from black-box quantization methods [15,16,20,69]. By virtue of our method being a full-wave method, here we do not construct the quantum Hamiltonian by fitting the impedance response of the system to a rational function, avoiding the introduction of uncontrollable errors. We also do not seek to synthesize a circuit that approximates the actual superconducting structure nor do we rely on the *ad hoc* classification of "qubitlike" modes and "cavitylike" modes. We sacrifice the simplicity brought about by these model reductions to obtain accurate mode structure and the full transparency in the ensuing quantization. In a multiscale system where the qubit is embedded in a cavity, a Josephson junction can be modeled by a single edge, in which case it is equivalent to a dipole. One can also choose to densely mesh the junction interface, and similarly the technique can handle a double or a triple junction, a long Josephson junction, a disordered piece of superconductor, or any geometry for a potential qubit candidate. Because it is rooted in how we linearize the nonlinear electrohydrodynamic equations to obtain the spectral problem for the hybridized field $\mathcal{A}$, the linearization of the qubit dynamics comes very naturally through the equation for $\mathbf{\Phi}$ defined everywhere and connects seamlessly with how the rest of the system is treated. Mode hybridization, i.e., the modification of the resonator modes due to the presence of the qubit and vice versa, is therefore also naturally captured simply by one solving the spectral problem. In this regard, the formulation is a generalization of the approach discussed in Ref. [18] for 1D circuits containing finite-size resonators. The observation that the interaction of the resonator with the qubit can significantly modify their coupling to the external environment—a key realization needed to correctly quantify radiative losses—was also pointed out in earlier work by Bamba and Ogawa [41] using a similar Lagrangian analysis.

That being said, before the theory can be quantization-ready, a rigorous spectral theory for the coarse-grained quantities that can correctly account for radiative losses and mode hybridization, both in the eigenfrequencies and in the spatial profile of the modes (including and particularly on the open boundaries), is needed and is the focus of this paper. In the following sections, we demonstrate with specific examples how this is achieved in our approach.

IV. MODES OF CLOSED SUPERCONDUCTING SYSTEMS

A. Performance benchmarks for simplicial and cubical DEC

We are interested in solving Eq. (6) for the electromagnetic modes of systems composed of possibly spatially

disjoint superconducting structures. To numerically compute the modes of such systems, we derive the DEC equation corresponding to Eq. (6):

$$\sum_{e_0\in\partial(e_0^\dagger)}\sum_{e_1\in\partial(e_0^\dagger)}\frac{\Delta\ell(e_0)}{\Delta A(e_0^\dagger)}\mathbf{\Phi}(e_1) + \left(\overline{\frac{1}{\lambda_L^2}}(e^\dagger)-\overline{n^2}(e^\dagger)k^2\right)\frac{\Delta A(e^\dagger)}{\Delta\ell(e)}\mathbf{\Phi}(e)=0, \quad (10)$$

where $\partial(e^\dagger)$ is the boundary of the dual face $e^\dagger$, and $\{\overline{1/\lambda_L^2},\overline{n^2}\}$ are defined as in Eq. (9). This form is universal and is independent of the mesh elements used.

First, we investigate the numerical convergence of DEC equations using two types of elements: simplicial and cubical. Simplicial elements are generally the preferred choice for a meshing scheme that conforms to arbitrary superconducting domains. To analyze the convergence of simplicial meshing, we consider shapes of superconducting cavities for which analytical solutions are available. A good choice is a rectangular cavity, which conforms well to cubical elements. A comparison of the convergence of error for simplicial and cubical meshing would illustrate the efficacy of simplicial meshing.

Consider a three-dimensional rectangular cavity with dimensions $L_x = 1\,\text{cm}$, $L_y = 1.5\,\text{cm}$, and $L_z = 2\,\text{cm}$, where L_x, L_y, and L_z are the sizes of the cavity along x, y, and z directions, respectively. To allow direct comparisons with analytical solutions, we first assume the cavity walls are perfect superconductors ($\lambda_L \to 0$), so the tangential component of $\boldsymbol{\mathcal{A}}$ vanishes at the boundary. This is equivalent to the boundary condition

$$\mathbf{\Phi}(e_t) = 0, \quad (11)$$

where e_t is an edge lying tangentially on the cavity boundary. The eigenmodes of the cavity are computed with two choices of meshing: tetrahedral and cubical. The convergence with respect to analytical solutions is shown in Fig. 2. As shown in Fig. 2(a), the error in the eigenvalues $E = k^2$ of both mesh choices converges at the same rate as the number of edges N_e in the discretized domain increases. The effectiveness of simplicial DEC is therefore shown to be comparable to that of cubical DEC, even when it is applied to a geometry where cubical meshing has an advantage due to its elements sharing the same symmetry as the cavity. In Fig. 2(b), we study how simplicial DEC produces accurate solutions to the edge fields of the eigenmodes. Convergence to analytical solutions of the edge fields is achieved.

These results help justify our shift to using simplicial meshing onward, as its flexibility allows us to apply DEC to complicated, realistic structures where cubical symmetry is rarely present. Moreover, simplicial meshing allows

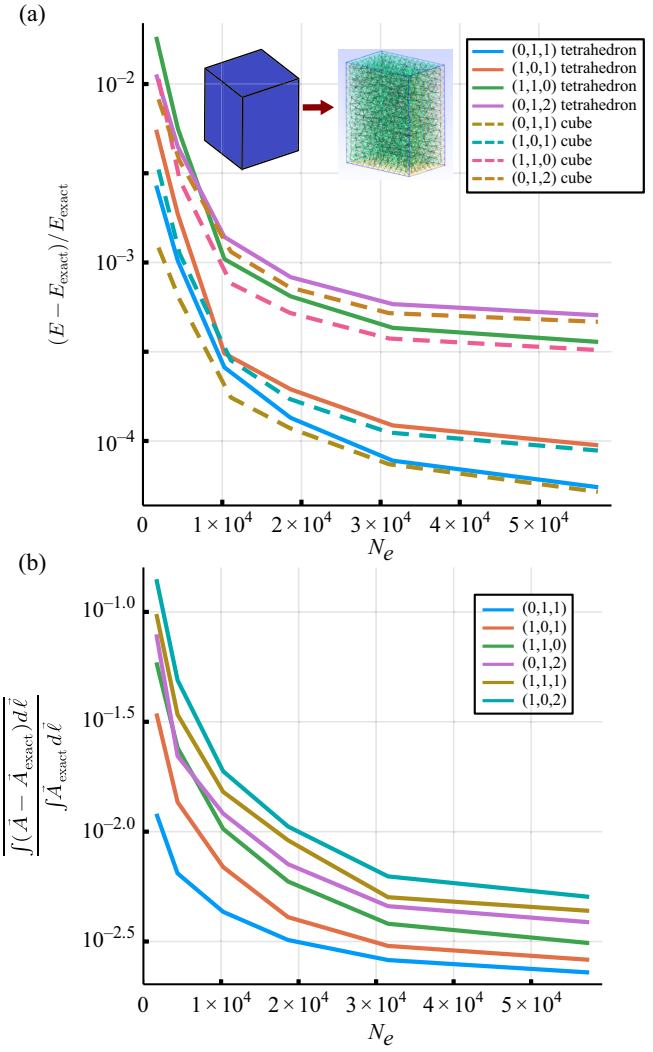

FIG. 2. (a) Convergence in the eigenvalues $E = k^2$ of the vector Helmholtz equation applied to a perfect superconducting cavity as a function of the number of edges N_e used in the discretization. The solid lines correspond to results obtained with simplicial meshing, while the dashed lines correspond to results obtained with cubical meshing. The relative error is calculated with respect to the exact analytical solution. (b) Relative error in the edge fields of the eigenmodes with respect to the analytical solutions. The errors are averaged over all edges and plotted as a function of N_e. The cavity dimensions are $L_x = 1$ cm, $L_y = 1.5$ cm, and $L_z = 2$ cm.

the implementation of different spatial resolutions in different regions, an important feature needed for the efficient application of DEC to systems comprising multiple spatial scales.

Next we consider a rectangular cavity enclosed by a superconducting shell that has a finite thickness. The penetration depth of this shell is set to be short enough so that the field inside the cavity decays immediately at the material interface, i.e., the inner walls of the cavity. Instead

of directly imposing the Dirichlet boundary condition at the cavity inner walls as in the previous case, we leave the values of the field floating there, and we impose only a "hard-wall" boundary condition [Eq. (11)] at the outer boundary of the shell, which is also the boundary of the computational domain. The purpose of this numerical experiment is to investigate the validity of DEC when there are sharp interfaces, such as the vacuum/superconductor boundary here, where the field undergoes abrupt variations. The procedure for applying material properties to the edges lying on the interface is given in Eq. (9). In a nonuniform tetrahedral mesh, the partitioning of the dual faces $e^{\dagger}$ that lie on multimaterial interfaces to the neighboring material domains is also highly nonuniform. This leads to the effective penetration depths of each edge on the same boundary being different from one another. One can imagine the vacuum/material interface made of many small patches, each with a slightly different material property, as shown in the top-right inset in Fig. 3. We compute the eigenmodes of Eq. (10) for an embedded cavity that has the same dimensional ratios as in the perfect cavity case; the convergence is shown in Fig. 3. The embedded cavity calculation achieves a similar order of accuracy as the perfect cavity calculation, and the two converge at the same rate as the mesh density increases.

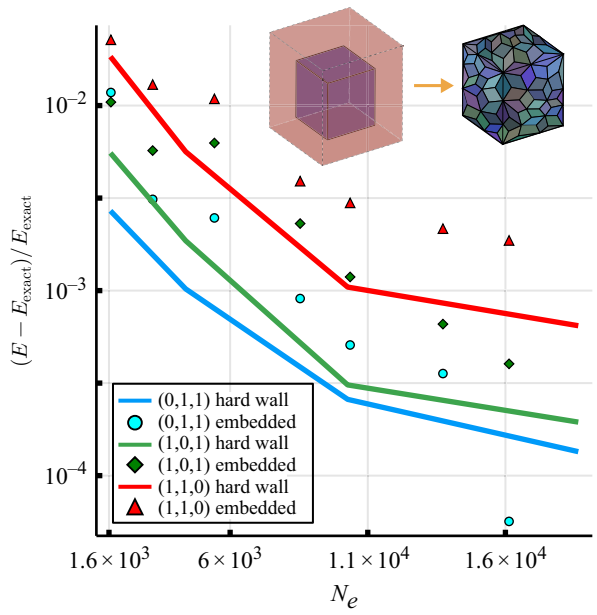

FIG. 3. Comparison between the convergence of computed eigenvalues for a cavity embedded in a superconducting shell and the convergence of computed eigenvalues for a perfect cavity with the hard-wall boundary condition imposed. N_e is the number of edges used in discretization of the cavity. The dimensions of the vacuum regions within both cavities are $L_x = 1$ cm, $L_y = 1.5$ cm, and $L_z = 2$ cm. A schematic of the embedded cavity is shown in the inset at the center top, while the inset in the top-right corner shows schematically how the effective penetration depth is assigned on the inner boundary of this cavity via coarse-graining.

B. Detection and removal of hybridization between degenerate modes

In symmetric structures such as the rectangular cavity discussed earlier in this article, there is a possibility of hybridization of degenerate modes in the numerically obtained eigenspectrum. These degeneracies are sometimes called "accidental" because they are not predicted by the symmetry group of the Hamiltonian but originate from a hidden symmetry of the system [74]. In such cases, numerical solvers tend to face difficulties in distinguishing these degenerate modes. For a rectangular superconducting cavity, the eigenvalues corresponding to each field component $\mathcal{A}_i$ of the field $\boldsymbol{\mathcal{A}}$ read

$$E_i \sim \left(\frac{n_x^2}{L_x^2} + \frac{n_y^2}{L_y^2} + \frac{n_z^2}{L_z^2}\right), \tag{12}$$

with the corresponding eigenfunction that is separable in Cartesian coordinates

$$\mathcal{A}_i = X_i(x)Y_i(y)Z_i(z). \tag{13}$$

If the ratio between any two of the three lengths L_x, L_y, or L_z is an integer, then there can be degeneracies. To numerically lift these degeneracies, the hidden symmetry needs to be eliminated. In this specific case, we can do so either by extending the cavity boundary to have a finite thickness, as was done in our earlier discussion on the embedded cavity, or by introducing a small perturbation of the cavity shape. To demonstrate this, we consider again the perfect cavity with dimensions $L_x{:}L_y{:}L_z = 1{:}1.5{:}2$. In Fig. 4(a), where the third and fourth modes of the unperturbed cavity are plotted, we can see that each field component of the two modes is characterized not by any single set of quantum numbers (n_x, n_y, n_z) but rather by a linear combination of the two accidentally degenerate modes. In Fig. 4(b), we plot the same modes, but the cavity is now slightly perturbed by an amount $\Delta L_z = 0.01$ along the z direction, so now $L_z' = L_z + \Delta L_z = 2.01$. The degeneracy is then lifted, and each of the two modes is now well-described by a distinct set of quantum numbers, which helps demonstrate the sensitivity of our numerical scheme to small changes in the geometry of the system simulated.

C. Calculations for closed multiscale systems

So far in this article, we have validated the accuracy of DEC by applying the method to simple systems with a large degree of symmetry and comparing the results with analytical solutions. The strength of DEC, however, lies in its ability to correctly capture the properties of systems containing multiple spatial scales through coarse-graining.

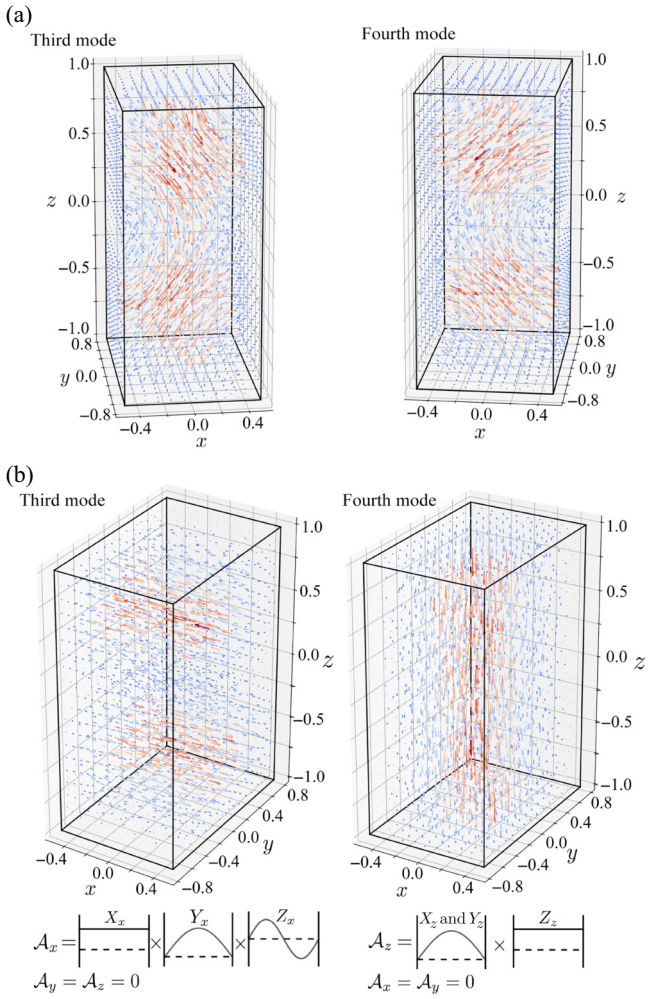

FIG. 4. Demonstration of the appearance and removal of hybridization between degenerate modes in a system with hidden symmetries. (a) The degenerate third and fourth modes of a rectangular cavity with perfect superconducting boundaries and dimension ratio of 1:1.5:2. (b) The third and fourth modes of a perturbed cavity when the dimension ratio is 1:1.5:2.01. The two modes are now well-characterized by their respective set of quantum numbers, which are schematically shown below the field distributions.

The ability to simulate the full multiscale system is especially important for analyzing package modes and how they affect the on-chip operations [53]—a study that requires a computational mesh capable of encompassing multiple spatial scales to cover the volume of the entire package while simultaneously resolving the fine details on the quantum chip. Another example of a multiscale system is a three-dimensional superconducting cavity containing one or a few superconducting chips. The dimensions of a 3D cavity are typically on the order of approximately 1 cm, while a dielectric substrate holding the qubits has a size of a few millimeters, and a qubit itself can have its smallest components in the range from micrometers to tens of nanometers. To model such systems, one possible workaround to avoid computational bottlenecks is to divide the problem into individual simulations of separate parts. However, because of hybridization, the spectral characteristics of the entire system composed of these devices being in the vicinity of each other can be vastly different from those of the individual components. Hence, it is imperative to be able to model the entire structure and directly extract its modes.

A schematic of the system we consider is shown in Fig. 5(a). It consists of a 3D cavity containing two dielectric substrates. A transmon qubit is mounted on each substrate. Each transmon qubit is composed of two superconducting capacitor pads connected by a Josephson junction. It is a well-known property of Josephson junctions that their dynamics are well-characterized by the coarse-grained phase across it [75]. In other words, to an observer outside and away from the junction and who can make measurements with only limited precision, the detailed dynamics inside the junction is unimportant to the dynamics that results from its interaction with the surrounding electromagnetic environment. This property can be used in coarse-grained calculations using DEC to reduce the complexity of the mesh needed; this is done by one modeling a junction by a single edge instead of finely meshing the junction geometry. In the calculations of electromagnetic modes, this is equivalent to the linearization of the junction across the edge. To obtain modes whose wavelengths are orders of magnitude larger than the longitudinal size of the junction, the fine details of the material distribution within the junction are irrelevant and do not need to be resolved during meshing. In Figs. 5(b)–5(e), a few example modes of this multiscale system are shown. In this calculation, we set the size of the cavity to be $1160 \times 160 \times 550$ mm^3, while the sizes of the two identical substrates are both $25 \times 50 \times 3$ mm^3 and they are separated by a distance of 600 mm. The size of the capacitor pads of the qubits is $6 \times 3 \times 0.1$ mm^3, and the two pads belonging to the same qubit are connected by a 0.2-mm-long bridge. We show the results for different types of mode that the system supports: In Figs. 5(b) and 5(c), single-qubit modes are shown, where the hybridization with the other qubit and the cavity field is suppressed. On the other hand, there can also be modes in which both qubits participate, such as the one shown in Fig. 5(d). Finally, in Fig. 5(e), we demonstrate a hybridized mode in which both the qubits and the cavity participate.

V. CALCULATIONS OF OPEN MODES

So far in this article, we have considered only closed systems, i.e., systems that support only modes that decay exponentially beyond their boundaries (e.g., a system surrounded by a superconducting enclosure much thicker than the relevant penetration depths). Here we extend DEC-QED to allow a mathematically rigorous consideration of

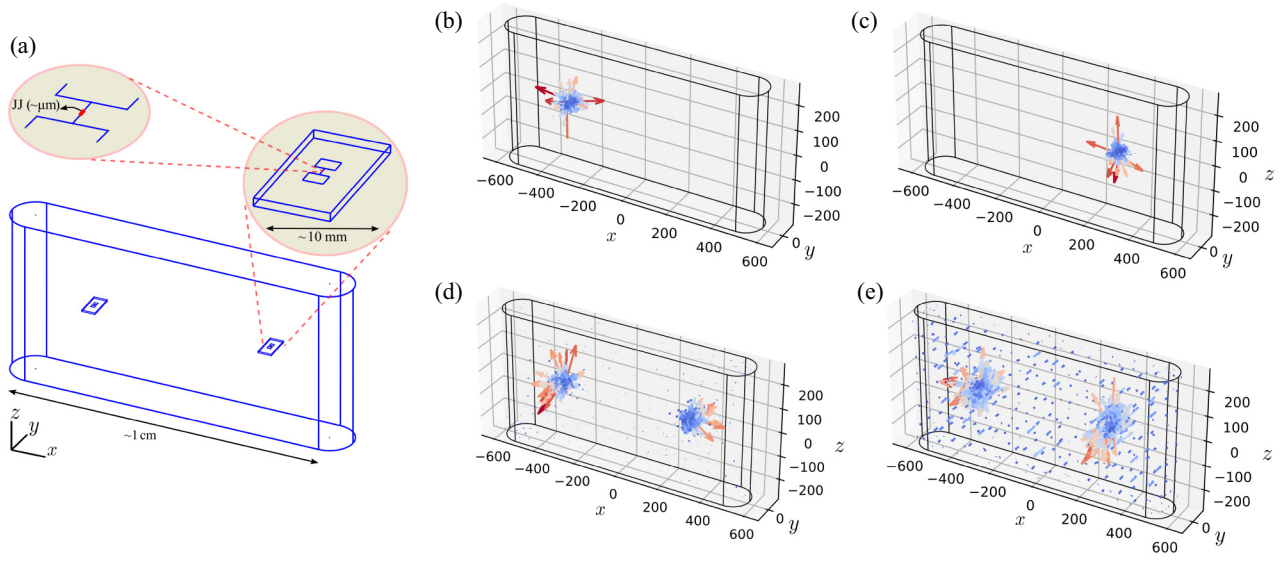

FIG. 5. (a) A system consisting of a three-dimensional superconducting cavity containing two spatially separated chips. Each chip is a dielectric substrate on top of which a Josephson qubit is mounted. The qubit is made of two superconducting capacitor pads connected together by a bridge containing a Josephson junction (JJ) of micrometer size. A few exemplary modes of the system are plotted, such as (b) the mode where only qubit 1 participates, (c) the mode where only qubit 2 participates, (d) the mode where both qubits are activated, and (e) a hybridization of the two qubits and the cavity field. The unit for all the axes in (b)–(e) is millimeters.

radiative losses. The correct modeling of open systems, where fields can propagate into and out of a confined domain, is of great interest since it is directly related to the quantification of qubit lifetimes and radiative losses. A superconducting qubit placed in an open cavity acquires a relaxation rate through hybridization of the qubit with the electromagnetic modes of the cavity. Therefore, its relaxation rate is given by the imaginary part of the complex-valued eigenfrequency of the qubitlike mode, while the difference between the real part in the frequency of a hybridized mode and the internal natural frequency of the qubit gives the Lamb shift [64]. In a similar vein, radiative loss of cavity modes is given by the imaginary parts of the cavitylike modes and is modified through hybridization with the qubit. Beyond the realm of superconducting microwave circuits, the problem has also been important to the broader scope of electromagnetic devices. We are particularly interested in the implementation of finite, open boundaries that are transparent so that fields can propagate through them without any reflection. Moreover, the formulation needs to be compatible with the eventual second quantization of the electromagnetic field everywhere within the system, including the boundary itself. Here we provide the derivations of two such approaches and present numerical demonstrations.

A. Green's boundary integral formulation for scalar fields

First, we discuss an implementation of open boundaries using Green's boundary integral formalism. The definition of radiative boundary conditions is analytically stated only at spatial infinity ($r \to \infty$). However, our goal is to state a mathematically equivalent condition at a finite distance from the cavity to keep the computationally volume as small as possible. We refer to this imaginary boundary that includes all material systems within its volume as the "surface of last scattering" (SOLS). We then use the analytically known free-space frequency-domain Green's function to "propagate" back the boundary condition at infinity to the SOLS chosen.

Consider a domain $\mathcal{D}$ consisting of possibly multiple disjoint regions all enclosed by an imaginary boundary surface. Before considering the spectral problem associated with the vector Helmholtz equation (6), we consider the warm-up problem of the Helmholtz equation for a scalar field $\phi(\mathbf{r})$:

$$\nabla^2\phi(\mathbf{r}) + n_i^2(\mathbf{r})k^2\phi(\mathbf{r}) = 0, \tag{14}$$

where $n(\mathbf{r})$ is the dielectric function of the ith region Γ_i, and k is again the wave number. The Green's function of the Helmholtz operator reads

$$G(\mathbf{r},\mathbf{r}',k) = \begin{cases} -\dfrac{i}{4}H_0^{(1)}(n_i k|\mathbf{r}-\mathbf{r}'|) & \text{in two dimensions,} \\ -\dfrac{e^{in_i k|\mathbf{r}-\mathbf{r}'|}}{4\pi|\mathbf{r}-\mathbf{r}'|} & \text{in three dimensions,} \end{cases} \tag{15}$$

where $H_0^{(1)}$ is the Hankel function of the first kind. At first glance, the Green's functions in Eq. (15) and their

derivatives diverging at $\mathbf{r} = \mathbf{r}'$ might seem to be a problem. This difficulty can be circumvented by one casting the boundary condition in an integral form to regularize the Green's function singularity [76,77]. On applying Green's second identity and taking the limit as $\mathbf{r}' \to \partial\Gamma_i$, we find that the field value at a point $\mathbf{r}'$ that lies on the boundary $\partial\Gamma_i$ of a domain is given by [71]

$$\phi(\mathbf{r}') = 2\mathcal{P}^{d-1}\int_{\partial\Gamma_i}\left[\phi(\mathbf{r})\nabla G(\mathbf{r},\mathbf{r}',k) - G(\mathbf{r},\mathbf{r}',k)\nabla\phi(\mathbf{r})\right]\cdot\mathbf{d}s, \tag{16}$$

where $\mathcal{P}^{d-1}$ indicates the $(d-1)$-dimensional Cauchy principal value integral, with d being the dimension of the domain. A detailed derivation of Eq. (16) is given in Appendix B for completeness. In Eq. (16), the field at a point on the boundary is determined by the field and its gradient everywhere else on the same boundary. Equation (16) is applicable to smooth boundaries of any form and shape. They can also be made up of different disjoint but closed segments.

To use Eq. (16) for application of the boundary condition at the domain boundary $\partial\mathcal{D}$, we need to numerically evaluate the normal gradient of the boundary field in a way that is self-contained within the field lying on the boundary itself. To do so, consider a secondary boundary $\partial\mathcal{D}'$ that is formed by one contracting $\partial\mathcal{D}$ by an amount Δr along the normal direction everywhere on the surface, as shown schematically in Fig. 6. There is now a thin layer bounded by $\partial\mathcal{D}\cup\partial\mathcal{D}'$ over which Green's identity can be performed to obtain Eq. (16) that determines $\phi(\mathbf{r}')$ for

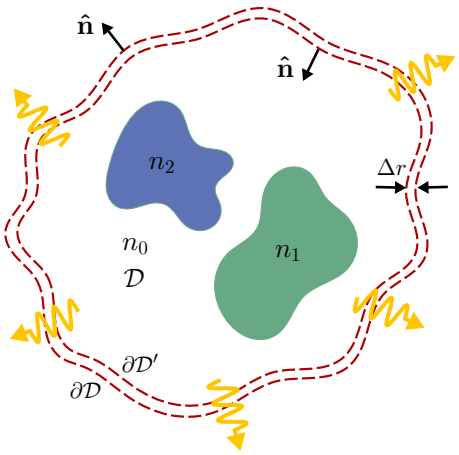

FIG. 6. An open system D consisting of multiple material regions with refractive indices n_i. The SOLS, the imaginary (transparent) boundary $\partial\mathcal{D}$ (the dashed contour) containing all material systems, can have an arbitrary shape as long as all regions of interest are enclosed within it. The secondary boundary $\partial\mathcal{D}'$ is created by one contracting everywhere the original boundary $\partial\mathcal{D}$ by an amount Δr.

every point $\mathbf{r}' \in \partial\mathcal{D}$. The surface integration is now done over $\partial\mathcal{D}\cup\partial\mathcal{D}'$. Note that during the evaluation of Eq. (16) the unit normal vector $\hat{\mathbf{n}}$ on $\partial\mathcal{D}'$ points into $\mathcal{D}$.

The application of open boundaries using Eq. (16) results in a boundary condition that depends parametrically on k. To solve for the eigenmodes of Eq. (14), we rewrite it as the following matrix representation:

$$\left[\mathbb{H}_s(k) + k^2\right]\mathbf{\Phi} = 0, \tag{17}$$

where $\mathbb{H}_s(k)$ is the scalar Helmholtz operator, and the vector $\mathbf{\Phi}$ contains the scalar field evaluated at all vertices in the computational mesh. The task of finding the eigenvalues of $\mathbb{H}_s(k)$ can be cast into a singular value decomposition problem [78]. The eigenvalues k_α correspond to locations of local minima in the lowest singular value of $\mathbb{M}_s(k) = \mathbb{H}_s(k) + k^2$.

We demonstrate the formulation presented here through calculations of the open modes of Eq. (14) applied to a 2D dielectric disk placed in a vacuum. The disk has radius $R_d = 5$ mm and $n = 1.5$, while the boundary is chosen to be a concentric circle with radius $R = 8$ mm. The results for the lowest singular value of $\mathbb{M}_s(k)$ are shown in Fig. 7(a) for k within the range $0 \le \mathrm{Re}(kR_d) \le 4\pi$ and $-3.5\pi \le \mathrm{Im}(kR_d) < 0$. Since the system supports incoming and outgoing modes equally, we need to focus only on the outgoing modes, whose real part of k is positive. The distribution of the eigenvalues has a mirror symmetry across $\mathrm{Re}(k) = 0$, and the incoming modes are different from the outgoing ones only by the sign of $\mathrm{Re}(k)$. The local minima in Fig. 7(a), whose locations correspond to the eigenvalues k_α, are collected and plotted in Fig. 7(b). Note that since all modes are radiative, their eigenvalues are complex, with the imaginary parts giving the corresponding relaxation rates. We also compare these numerically computed eigenvalues with the semianalytical solutions obtained by our solving the transcendental equation arising from matching the continuity condition of the field and its normal derivative at the edge of the disk. As seen in Fig. 7(b), the numerically obtained eigenvalues (orange) agree with the eigenvalues obtained through the analytical equation (blue) over a wide range of k.

The field distributions of a few eigenmodes are presented in Fig. 8, where the real part of the fields, $\mathrm{Re}(\phi)$, is plotted. The numerical labeling of the modes is done first in ascending order of $\mathrm{Im}(k_\alpha R_d)$ in the range $\{-3.5\pi, 0\}$, then in ascending order of $\mathrm{Re}(k_\alpha R_d)$ in the range $\{0, 4\pi\}$. The features exhibited by these distributions can be understood through analytical considerations; in polar coordinates, one can write the fundamental solution to the scalar Helmholtz equation as $\phi(r,\theta) = R(r)\Theta(\theta)$. The angular dependence of the fields is of the form $\Theta(\theta) \sim e^{\pm im\theta}$, which is confirmed by the curves in red in Fig. 8, where the angular dependence of the fields is plotted at a fixed radius. The radial component, on the other hand, is given

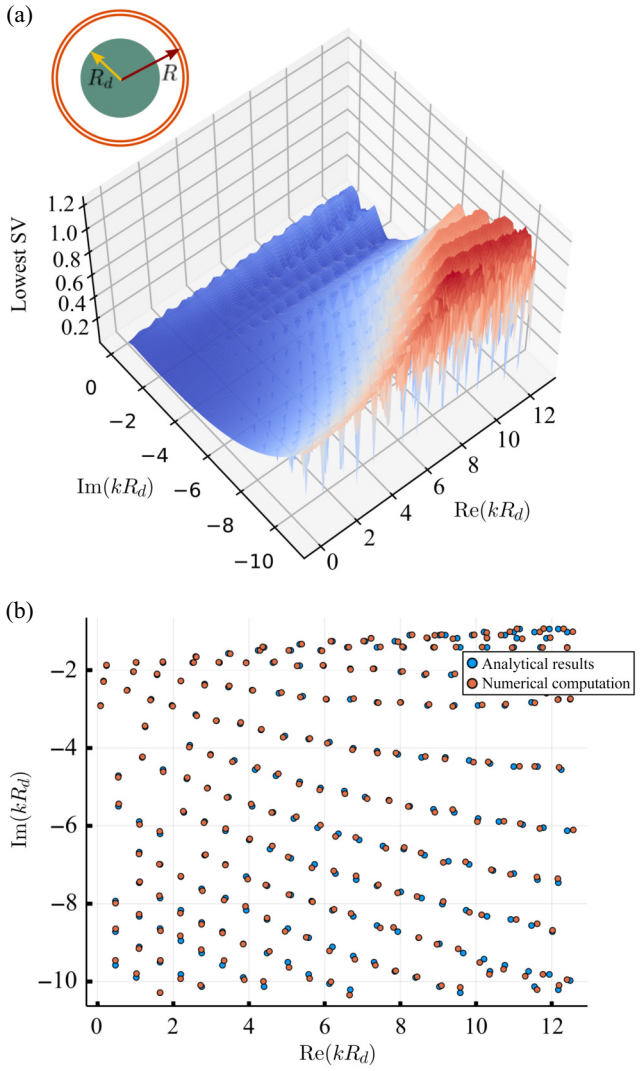

FIG. 7. (a) Lowest singular value (SV) of $\mathbb{M}_s(k)$ computed for a sample range of k. The physical system is a dielectric disk with radius $R_d = 5$ mm and refractive index $n = 1.5$. A schematic of the system is given in the top-left corner. (b) The eigenvalues k_n of $\mathbb{H}_s(k)$ are indicated by the locations of the local minima of the lowest singular value of $\mathbb{M}_s(k)$. The semianalytical results are plotted in blue, while the numerically computed values are plotted in orange.

by $R(r) \sim Z_m(nkr)$, where Z_m is the Bessel function of the first kind J_m, the Bessel function of the second kind Y_m, or the Hankel functions $H_m^{(1,2)}$. Inside the dielectric disk, the radial component of the field is given by J_m, while the field outside the disk is described by $H_m^{(1)}$ $\left(H_m^{(2)}\right)$ for an outgoing (incoming) wave. This radial dependence is shown by the blue curves in Fig. 8.

B. Green's boundary integral formulation for vector fields

A problem of greater interest is, however, the implementation of open boundaries for vector fields. For this, we have extended Green's boundary integral method for scalar fields to address the vector Helmholtz problem as well. Consider a divergence-free vector field $\boldsymbol{\mathcal{A}}(\mathbf{r}')$ that satisfies Eq. (6) defined over the domain $\mathcal{D}$. The dependence of the field value at a location $\mathbf{r}' \in \partial D$ on the field everywhere else on the same boundary is given by

$$\boldsymbol{\mathcal{A}}(\mathbf{r}') = -2\mathcal{P}^{d-1}\int_{\partial D}\Big\{G(\mathbf{r},\mathbf{r}',k)\left[(\nabla\times\boldsymbol{\mathcal{A}})\times\hat{\mathbf{n}}\right] - \nabla G(\mathbf{r},\mathbf{r}',k)(\boldsymbol{\mathcal{A}}\cdot\hat{\mathbf{n}}) - \nabla G\times(\boldsymbol{\mathcal{A}}\times\hat{\mathbf{n}})\Big\}\,ds, \tag{18}$$

where $G(\mathbf{r},\mathbf{r}',k)$ is again the scalar Green's function as defined in Eq. (15), and the principal value integral is generalized to the vector case. A detailed derivation of Eq. (18) is given in Appendix B.

We demonstrate the implementation of the boundary condition in Eq. (18) in DEC by calculating the modes of Eq. (6) applied to the same 2D dielectric disk studied in the scalar case. Consider a discretization of the computational domain into a polar grid that has N_R and N_θ vertices along each radial ray and circle, respectively. In the case of the open BC, it is natural to allow the mesh to also be "open" such that there are additional edges on the physical boundary of the system that protrude outward in the direction normal to the surface, as shown in Fig. 9(a). A primal edge e in this setup is identified by n_r and n_θ, its radial and angular indices, accompanied by a superscript r or θ indicating the direction of the edge. In DEC, the application of BCs to a vector field translates to the application of BCs for the normal and tangential edge fields $\boldsymbol{\Phi}(e^r_{N_R,n_\theta})$ and $\boldsymbol{\Phi}(e^\theta_{N_R,n_\theta})$ lying on the boundary edges. The condition in Eq. (18), when applied to a 2D circular boundary, then becomes

$$\boldsymbol{\Phi}(e^r_{N_R,n_\theta}) = -\boldsymbol{\Phi}(e^r_{N_R-1,n_\theta}) + \sum_\theta 2\left\{\frac{\partial G}{\partial r}\left[\boldsymbol{\Phi}^r_{N_R+1}(\theta)+\boldsymbol{\Phi}^r_{N_R}(\theta)\right]R\Delta\theta - \frac{\partial G}{\partial\theta}\left[\boldsymbol{\Phi}^\theta_{n_\theta-1}(R)+\boldsymbol{\Phi}^\theta_{n_\theta}(R)\right]\frac{\Delta R}{R}\right\} \tag{19}$$

for the radial boundary edge, and

$$\boldsymbol{\Phi}(e^\theta_{N_R,n_\theta}) = -\boldsymbol{\Phi}(e^\theta_{N_R,n_\theta-1}) - \sum_\theta\Bigg\{2\Delta\theta\left[G(\mathbf{r},\mathbf{r}',k)\left(1+\frac{R}{\Delta R}\right)-R\frac{\partial G}{\partial r}\right]\times\left(\boldsymbol{\Phi}^\theta_{n_\theta}(R)+\boldsymbol{\Phi}^\theta_{n_\theta-1}(R)\right) - 2G\frac{R\Delta\theta}{\Delta R}\left(\boldsymbol{\Phi}^\theta_{n_\theta}(R-\Delta R)+\boldsymbol{\Phi}^\theta_{n_\theta-1}(R-\Delta R)\right) - 2R\frac{\Delta\theta^2}{\Delta R}\frac{\partial G}{\partial\theta}\left[\boldsymbol{\Phi}^r_{N_R+1}(\theta)+\boldsymbol{\Phi}^r_{N_R}(\theta)\right]$$

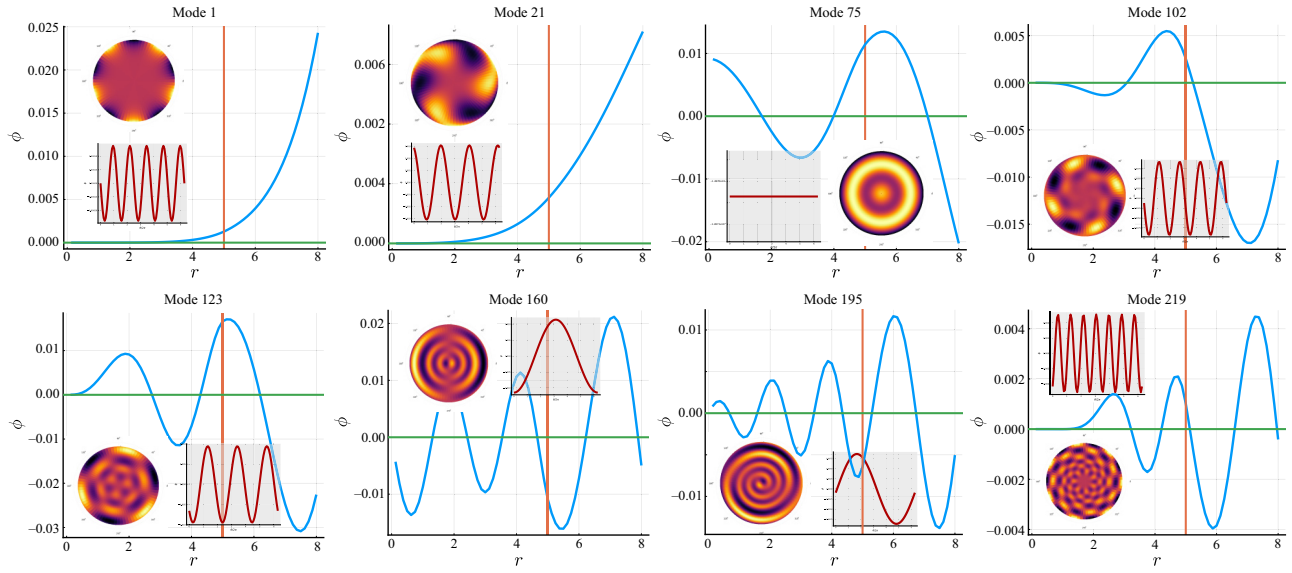

FIG. 8. Selection of open modes of the scalar Helmholtz equation on a dielectric disk whose radius $R_d = 5$ mm and refractive index $n = 1.5$. In each panel, the surface plot shows the distribution of $\mathrm{Re}(\phi)$ in the entire domain inside the boundary radius R. The blue curve shows the value of $\mathrm{Re}(\phi)$ at fixed angle $\theta = 4\pi/5$ as a function of the radial coordinate r. The unit for the horizontal axes is millimeters. The vertical orange line indicates the edge of the disk. The red curve shows the field at fixed radius $r = 4$ as a function of the angular coordinate θ.

$$- G\frac{R\Delta\theta}{\Delta R}\left[\mathbf{\Phi}^r_{N_R+1}(\theta+\Delta\theta) + \mathbf{\Phi}^r_{N_R}(\theta+\Delta\theta) - \mathbf{\Phi}^r_{N_R+1}(\theta-\Delta\theta) - \mathbf{\Phi}^r_{N_R}(\theta-\Delta\theta)\right]\Bigg\} \quad (20)$$

for the angular boundary edges, where ΔR and $\Delta\theta$ are the spacing between consecutive grid points on a radial ray and a circle, respectively.

Similarly to the scalar problem, to search for the eigenvalues, we compute the lowest singular values of the operator $\mathbb{M}_v(k) = \mathbb{H}_v(k) - k^2$, where $\mathbb{H}_v(k)$ is the vector Helmholtz operator. The distribution of the local minima of $\mathbb{M}_v(k)$ in k-space is shown in Fig. 9(b). The field distributions of a few randomly selected eigenmodes are presented in Fig. 9(c), where the plotted vector fields exhibit the correct behavior of how radiations permeate and escape a dielectric disk.

To demonstrate the versatility of DEC in computing radiative modes of arbitrarily shaped systems, we apply the formulation to the modeling of a superconducting qubit chip placed in the region between two cylindrical capacitors, as schematically shown in Fig. 10(a). The qubit is made of two superconducting islands that are separated by a distance of 0.75 mm and connected by a bridge that contains a Josephson junction. The width of both the bridge and the junction is 50 μm, and the qubit is mounted on a circular dielectric disk that has radius $R_d = 4$ mm with refractive index $n = 1.5$. We assume the two ideal superconducting cylindrical capacitors extend indefinitely toward both ends, and the qubit is placed in the middle of the slit separating them. The width h of the vacuum spacing between the two cylinders is taken to be very small compared with their radius R_c. This allows us to effectively discretize the distance between the surfaces of the two cylinders by two edges. Because of mirror symmetry at $z = 0$, the amplitude of the coarse-grained field on one z edge is identical to that of its mirroring edge. This allows us to decouple the in-plane field component from the out-of-plane component, and we can focus on solving for the modes of Eq. (10) applied to the 2D in-plane field on the $z = 0$ slice, where the substrate containing the qubit is located. We choose the computational boundary to be a circle whose radius $R = 8$ mm is half that of the cylindrical capacitors R_c. There are two notable types of mode, for which examples are shown in Figs. 10(b) and 10(c). Because of the geometry of the qubit being two islands connected by a bridge, it can act as a dipole. A mode that behaves in this way is shown in Fig. 10(b), where the field lines exit in the normal direction from one island and enter the other island. The field also decays in the bulk of the islands at a rate determined by their penetration depths. In another scenario, because of their separation, the two islands can behave as individual superconducting objects around which the field lines flow with no normal component at the surfaces of the islands. A demonstration of such a mode is shown in Fig. 10(c). Finally, in Fig. 10(d), we show how one can tune the internal resonance frequency of the qubit through a cavity resonance, exposing the Purcell

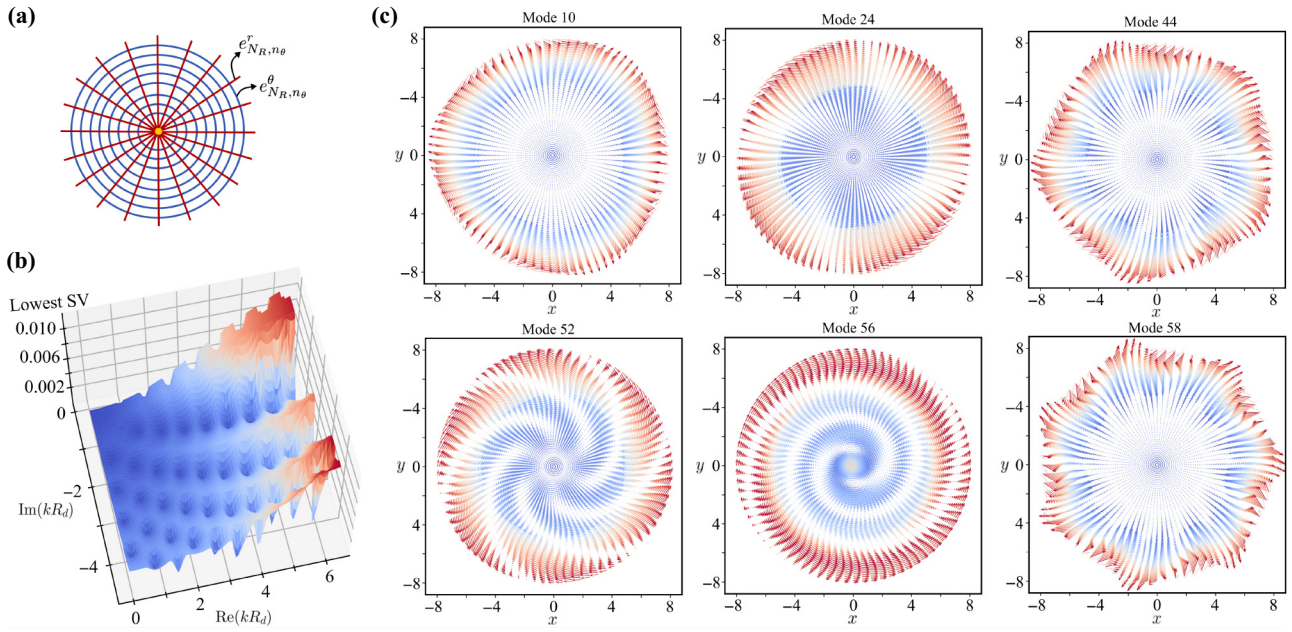

FIG. 9. Open-mode calculations of the vector Helmholtz problem for a dielectric disk placed in a vacuum. The disk has radius $R_d = 5$ mm and refractive index $n = 1.5$. (a) The polar grid used in the calculation. (b) Surface plot of the lowest singular value (SV) of the operator $\mathbb{M}_v(k)$ as a function of k. The local minima indicate the eigenvalues of the vector Helmholtz operator $\mathbb{H}_v(k)$. (c) Distributions of Re($\boldsymbol{\mathcal{A}}$) in a number of radiative modes (the unit for all axes is millimeters).

enhancement of the qubit relaxation rate [63]. The relaxation rate due to radiative loss of a qubitlike mode, i.e., the spontaneous emission rate, is plotted as a function of the qubit frequency. We observe a finite peak as the qubit frequency is resonant with a cavitylike mode, signifying an increased emission rate due to the hybridization of this qubit mode with the cavity field [43]. In this case, the Purcell enhancement factor with respect to its value away from resonance is not large, because we intentionally chose a very (radiatively) lossy cavity represented by our placing two cylinders facing each other, a situation that corresponds to the regime of overlapping resonances (finesse much less than 1).

As mentioned earlier, the formulation for calculating radiative fields using the Green's function method is flexible in terms of the shape and topology of boundary surfaces to which it can be applied. The physical boundary of the system can be made of multiple, possibly disjoint, but closed segments that bound a non-simply-connected structure. However, the vector field being calculated has to be divergence-free as a prerequisite. Although this restriction is not a concern in many useful cases, such as the calculation of the electric field in a sourceless region or of the magnetic vector potential in the Coulomb gauge, it is sometimes helpful to have the freedom of not necessarily having to choose a divergenceless field. In the following section, we introduce an alternative formulation that achieves this.

C. Vector spherical harmonics expansions

In this section, we discuss the implementation of open boundaries using VSH expansions. VSH [79] are an extension for vector fields of scalar spherical harmonics. There are three subclasses of these vectors, defined in spherical coordinates (r, θ, φ) as

$$\mathbf{Y}_{lm} = Y_{lm}(\theta, \varphi)\hat{\mathbf{r}}, \tag{21}$$

$$\Psi_{lm} = r\nabla Y_{lm}(\theta, \varphi), \tag{22}$$

$$\mathbf{\Phi}_{lm} = \mathbf{r} \times \nabla Y_{lm}(\theta, \varphi) \tag{23}$$

that altogether form an orthonormal and complete basis. Any vector field can then be expanded as follows:

$$\boldsymbol{\mathcal{A}}(\mathbf{r}) = \sum_{l=0}^{\infty} \sum_{m=-l}^{l} \mathcal{A}^r_{lm}\mathbf{Y}_{lm} + \mathcal{A}^{(1)}_{lm}\Psi_{lm} + \mathcal{A}^{(2)}_{lm}\mathbf{\Phi}_{lm}, \tag{24}$$

where the coefficients $\mathcal{A}^r_{lm}$, $\mathcal{A}^{(1)}_{lm}$, and $\mathcal{A}^{(2)}_{lm}$ are functions of the radial coordinate r. In Eq. (24), of the three mutually orthogonal terms, the first term on the right-hand side is the radial component of the field, while the remaining two terms are angular contributions. Note that neither of the angular terms aligns with azimuthal or polar directions but is a linear combination of both. Using Eq. (24) as an ansatz for the field, we can split Eq. (6) into three decoupled ordinary differential equations, each for one of the

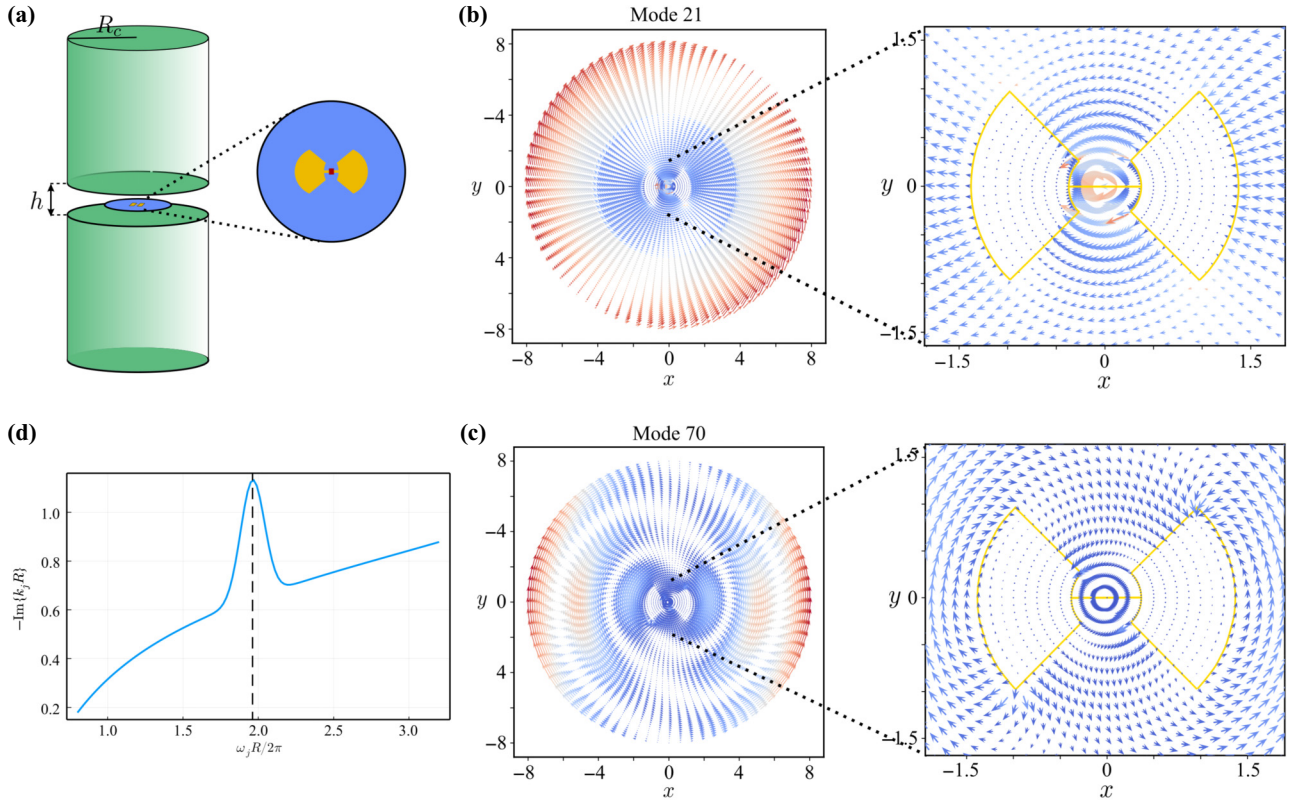

FIG. 10. Calculations of radiative modes of a transmon qubit sandwiched between two cylindrical superconducting capacitors. (a) The system considered. The qubit is mounted on a circular dielectric disk with radius $R_d = 4$ mm and refractive index $n = 1.5$. The qubit is composed of two superconducting islands that are 0.75 mm from each other and connected by a bridge containing a junction in the middle. The width of both the bridge and the junction is 50 μm. (b) Example of a "dipole" mode. The qubit acts like a dipole, with the field lines starting from the surface of one island and ending on the surface of another island. (c) Example of a mode where the field lines flow around the individual capacitor islands with no normal component at each island's surface. The boundary of the qubit is shown in yellow in the enlarged insets, and all the axes of the plots have the unit of millimeters. (d) Spontaneous emission rate of a qubitlike mode as a function of the qubit frequency.

three coefficients. Their solutions are

$$\mathcal{A}^r_{lm} = \frac{Z_{l+1/2}(kr)}{r^{3/2}}, \tag{25}$$

$$\mathcal{A}^{(1)}_{lm} = \frac{1}{\mathrm{i}(l+1)}\left\{\frac{Z_{l+1/2}(kr)}{r^{3/2}} + \frac{k}{\sqrt{r}}\left[Z_{l-1/2}(kr) - Z_{l+3/2}(kr)\right]\right\}, \tag{26}$$

$$\mathcal{A}^{(2)}_{lm} = \frac{\pi}{2kr} Z_{l+1/2}(kr), \tag{27}$$

where Z, in general, can be the Bessel function of the first kind J, the Bessel function of the second kind Y, or the Hankel functions $H^{(1,2)}$. For the outgoing (incoming) waves, the Hankel functions of the first (second) kind provide the appropriate description. After the VSH expansion in Eq. (24), the implementation of the open boundary condition on the field $\boldsymbol{\mathcal{A}}$ now reduces to the BC on each of the three field components $\boldsymbol{\mathcal{A}}^r$, $\boldsymbol{\mathcal{A}}^{(1)}$, and $\boldsymbol{\mathcal{A}}^{(2)}$. Here we discuss the BC for $\mathcal{A}^r$ as an example, while the details for the BCs for $\mathcal{A}^{(1)}$ and $\mathcal{A}^{(2)}$ are given in Appendix C.

Consider a spherical boundary of radius R. The series expansion for the radial component of the radiating field on the sphere is given by

$$\boldsymbol{\mathcal{A}}^r(R,\theta,\varphi) = \sum_{l,m} \tilde{a}^r_{lm} A^r_{lm}(R)\mathbf{Y}_{lm}(R,\theta,\varphi) = \sum_{l,m} \tilde{a}^r_{lm} \frac{H_{l+1/2}(kR)}{R^{-3/2}} Y_{lm}\hat{\mathbf{r}}, \tag{28}$$

where $\tilde{a}^r_{lm}$ are the expansion coefficients. Performing integration over the surface of the sphere and using the orthonormality condition of VSH, we arrive at an expression for the expansion coefficients as follows:

$$a^r_{lm} \equiv \tilde{a}^r_{lm} H_{l+1/2}(kR)$$

$$= R^{3/2} \int d\Omega \boldsymbol{\mathcal{A}}^r \cdot \mathbf{Y}^*_{lm}$$
$$= R^{-1/2} \sum_{i,j} \mathcal{A}^r(R, \theta_i, \varphi_j) Y^*_{lm}(\theta_i, \varphi_j) \Delta A(f), \quad (29)$$

where $\int d\Omega$ is the solid angle integral that covers the entire sphere, and the last line of Eq. (29) is the discretized version of the integral written as a sum over all the triangular patches f whose centers are located at (θ_i, φ_j) on the spherical boundary. To apply the BCs, consider the sphere beneath the boundary that has radius $R - \Delta r$ (i.e., the second-to-last layer). The radial derivative of $\mathcal{A}^r$ is given by

$$\frac{\mathcal{A}^r(R,\theta,\varphi) - \mathcal{A}^r(R-\Delta R,\theta,\varphi)}{\Delta R} = \sum_{l,m} \tilde{a}^r_{lm} \left[\frac{-3}{2R^{5/2}} H_{l+1/2}(kR) + \frac{k}{R^{3/2}} H'_{l+1/2}(kR) \right] Y_{l,m}, \quad (30)$$

which allows us to write the field at the boundary $\mathcal{A}^r(R, \theta, \varphi)$ in terms of the expansion coefficients $\tilde{a}^r_{lm}$ and the field at the layer with radius $R - \Delta R$. Using Eq. (30) and the expression for $\tilde{a}^r_{lm}$ derived in Eq. (29), we find that the boundary condition for $\mathcal{A}^r$ is then

$$\mathcal{A}^r(R,\theta,\varphi) = \sum_{l.m} \sum_{i,j} \mathcal{A}^r(R-\Delta R,\theta_i,\varphi_j) Y^*_{lm}(\theta_i,\varphi_j) \frac{\Delta A(f)}{R^2} \times \left\{ 1 + \Delta R \left[-\frac{3}{2R} + k \frac{H_{l-1/2}(kR) - H_{l+3/2}(kR)}{2H_{l+1/2}(kR)} \right] \right\} \times Y_{lm}(\theta,\varphi). \quad (31)$$

Equation (31) is for the radial component of the field, which in DEC is a scalar lying on vertices of the primal mesh. To arrive at the appropriate BC for the edge field $\mathbf{\Phi}(e)$ governed by the discrete vector Helmholtz equation given in Eq. (10), we need to rewrite $\mathcal{A}^r(R, \theta, \varphi)$ and $\mathcal{A}^r(R - \Delta R, \theta_i, \varphi_j)$ in terms of the edges belonging to the vertex located at (R, θ, φ). This means two consecutive spherical layers beneath the boundary are needed to compute $\mathcal{A}^r(R - \Delta R, \theta_i, \varphi_j)$. The procedure as a whole can be substantially simplified by one designing the mesh so that the boundary surface and the two layers beneath it have identical triangulation patterns. This ensures that for any vertex v_b located at (R, θ, φ) on the boundary surface, there is an edge e^r oriented radially that connects v_b with the vertex v'_b at $(R - \Delta R, \theta, \varphi)$ that has the same angular coordinates as v_b. Similarly, there is always an edge connecting v'_b with a vertex v''_b at $(R - 2\Delta R, \theta, \varphi)$. Note that we need only the three outermost layers of the mesh to be spherical and have identical triangulation patterns, while the rest of the internal domain can be freely and randomly discretized with tetrahedra. Similarly to the discussion on the Green's function approach in the previous section, here, for open boundaries, it is convenient to use an open mesh such that there are radial edges that protrude out of the boundary surface. The BC applied to these boundary radial edges e^r_b is then

$$\mathbf{\Phi}(e^r_b) = -\mathbf{\Phi}(e^{r'}_b) + \sum_{e^r} \sum_{f \supset v | v \subset e^r} \sum_{l,m} \frac{\Delta A(f)}{3R^2} \mathbf{\Phi}(e^r) \times \left\{ 1 + \Delta R \left[-\frac{3}{2R} + k \frac{H_{l-1/2}(kR) - H_{l+3/2}(kR)}{2H_{l+1/2}(kR)} \right] \times Y^*_{lm}(f) Y_{lm}(\theta,\varphi) \right\}, \quad (32)$$

where $e^{r'}_b$ is the other radial edge that shares the boundary vertex with e^r_b. In Eq. (32), the first sum is done over all radial edges e^r lying in the two layers beneath the boundary surface, while the second sum is done over all faces f that share a vertex with e^r. This concludes our derivation for the open BC applied to a radial edge in the DEC framework. The boundary conditions for edges lying tangential to the surface are discussed in Appendix C.

We apply the formulation developed here to calculate the modes for a three-dimensional dielectric microsphere surrounded by a vacuum. The radius R_d of this dielectric sphere is kept fixed at 12 μm throughout all calculations discussed in this section. The computational boundary is an "imaginary" spherical surface at finite radius $R > R_d$, as schematically shown in Fig. 11(a). The results of the eigenvalue search found through singular value calculations are shown in Fig. 11(b), where we chose $R = 24$ μm. With a primal mesh of approximately 2900 vertices and approximately 18 000 edges, the local minima of the smallest singular value are on the of order 10^{-7}, proving them to be reliable indicators of the eigenvalues of the system. The dielectric microsphere is chosen to demonstrate our formulation because there exist semianalytical solutions that can be obtained by one solving the transcendental equation arising from enforcing the continuity of the field and its normal derivative at the dielectric/vacuum interface. We use these solutions to investigate the efficacy of our method in a number of ways. First, the numerical implementation of the series expansion in Eq. (28) requires a truncation of the number of terms considered. We, therefore, investigate the dependence of the convergence rate on the number of Bessel functions included while keeping the mesh size fixed. The results can be seen in Fig. 11(c), where we show the error of the numerically obtained lowest eigenvalue computed with the semianalytical solution. With a manageable number of $L_{\max} = 10$, where $L_{\max}$ is the largest ordering of Bessel terms in the expansion, the error reduces to below 4%. Another important factor is how large the

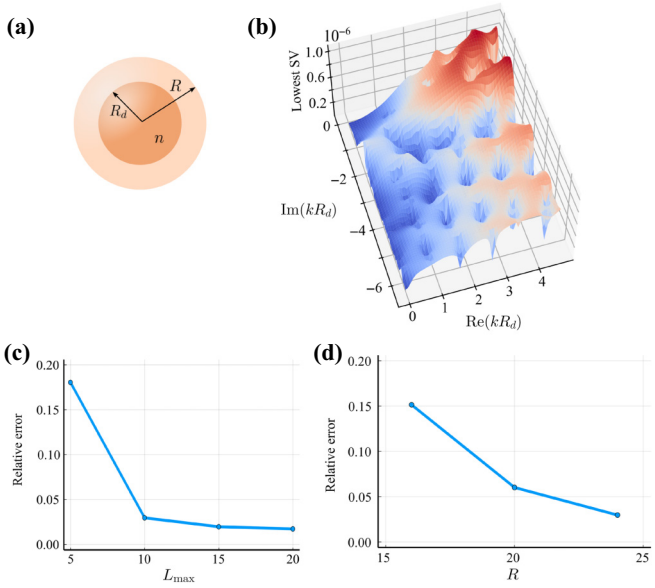

FIG. 11. Results for the open-boundary modes of a dielectric microsphere. (a) The system studied: a sphere of radius $R_d = 12\ \mu\mathrm{m}$. (b) Lowest singular value (SV) of $\mathbb{M}_v(k)$ as a function of k. (c) Error of the lowest eigenvalue as a function of the largest ordering of Bessel terms. (d) Error of the lowest eigenvalue as a function of the boundary radius R.

computational boundary needs to be in order to achieve precise solutions, since accuracy is expected to increase as the boundary is moved further away from where the devices are concentrated, but one doing so also increases the mesh complexity, and hence the computational burden is increased. In Fig. 11(d), the convergence as a function of the boundary radius R of the lowest eigenvalue is plotted. We see that even with a tight boundary when $R = 16\ \mu\mathrm{m}$ (while the dielectric sphere is kept at $12\ \mu\mathrm{m}$) the error is relatively low at 15%, and for $R = 2R_d$, it is reduced to below 4%. These results verify that our coarse-grained implementation of open boundaries using VSH is able to produce accurate solutions using a boundary of reasonable size.

The formulation based on VSH expansions introduced here allows effective calculations of open modes while also removing the requirement of divergenceless fields. However, unlike Green's boundary integral formulation, which is adaptable to arbitrarily shaped boundaries, this approach needs to be implemented on a spherical surface. This makes the formulation most suitable when applied to three-dimensional structures that have comparable lengths along the three directions, such as 3D cavities. In some other specialized cases, this requirement may limit us from drawing the tightest boundary possible, which, in turn, might cause the computational domain to be larger than it needs to be. An example is a coplanar waveguide whose length is much larger than its planar width, which, in turn, is much larger than the thickness along the cross section of the waveguide. In such a case, replacement of a spherical boundary with an ellipsoidal one is preferable since an ellipsoid has three tuning parameters that allow squeezing and stretching in three directions. Fortunately, the series expansion–based approach discussed here is extendable to ellipsoidal coordinates. This relies on the fact that the Helmholtz equation is separable in ellipsoidal coordinates as well, which allows the expansion of functions, now in terms of ellipsoidal waves. Although a mathematically intensive discussion on how to generalize our method to ellipsoidal coordinates is beyond the scope of this article, in Appendix D we provide a preamble by discussing a brief proof of the separability of the Helmholtz equation.

VI. CONCLUSION

In this article, we have introduced a spectral theory for the modeling of mode hybridization and relaxation rates in general systems composed of superconducting and dielectric materials. In doing so, we have demonstrated the following important points:

(1) We have shown that the coarse-grained formulation of electrodynamics using discrete exterior calculus is adaptable to simplicial and complex meshing strategies with equal precision. Although based on the calculations of coarse-grained quantities, the numerical scheme can still display the high sensitivity to small changes in the geometry and topology of the system that is needed, for instance, in the categorization of degenerate modes arising from hidden symmetries when a small perturbation is introduced.

(2) The method, which maps the problem of modeling vector fields to the calculation of averaged projections lying on discrete edges, is particularly effective when applied to systems composed of objects of multiple spatial scales, such as those used in superconducting electronic circuits. Since the method keeps track of the average variables, it allows more-efficient meshing strategies that take into account the sizes of the Josephson junctions as well as the finite resolution imposed by a given measurement apparatus. This is an important advantage that this formulation offers because here the mesh does not need to be finer than the size of the Josephson junctions or the measurement apparatus. Future work will focus on adaptive meshers that adapt to the finite spatiotemporal resolution provided by the measurement apparatus interrogating a particular dynamics, allowing the efficient and accurate simulation of only what is measurable.

(3) We have introduced two implementations of open boundaries for the vector wave equation that are applicable to a wide range of electromagnetic systems. By drawing "imaginary," transparent boundaries that are reasonably sized, we are able to faithfully produce the open modes that agree well with analytical solutions. We also demonstrated

the flexibility of the formulation by applying it to the calculation of radiative modes of a superconducting qubit.

(4) Because the formulation we developed deals with the gauge-invariant field that hybridizes light and matter and pervades the entire system, solving the spectral problem associated with it naturally gives us modes that hybridize all the modes of individual components in the circuit.

The spectral theory presented here is suitable for the second quantization of the electromagnetic field and the time-dependent numerical simulation of the nonlinear dynamics of open superconducting systems with arbitrary complexity. We expect the ability to accurately and efficiently extract relaxation rates, as well as the quantification of mode hybridization demonstrated here, to be useful in the modeling and optimization of superconducting circuits.

ACKNOWLEDGMENTS

We gratefully acknowledge discussions with Nicholas Bronn, Thomas G. McConkey, Anil N. Hirani, Thomas Maldonado, Zoe Zager, and Haley M. Cole. We are grateful to Benjamin Lienhard and Wentao Fan for their critical reading of the paper and their insightful comments. We acknowledge support from the U.S. Department of Energy, Office of Basic Energy Sciences, Division of Materials Sciences and Engineering, under Award No. DESC0016011. The simulations presented in this article were performed on computational resources managed and supported by Princeton Research Computing, a consortium of groups including the Princeton Institute for Computational Science and Engineering and the Office of Information Technology's High-Performance Computing Center and Visualization Laboratory at Princeton University.

DATA AVAILABILITY

All the data presented in this paper are generated through numerical simulations. The theoretical framework for obtaining the results is thoroughly explained within the paper, and the computational toolbox used for the calculations is available in our publicly accessible open-source repository, which has been referenced earlier in the paper.

APPENDIX A: LINEARIZATION OF THE EHDS EQUATIONS

In this appendix, we provide a derivation for the linearization of the EHDS equations that leads to the spectral problem analyzed in this article. We start with the gauge-invariant form of the EHDS equations [Eqs. (4) and (5)] and impose the condition that charge conservation is individually respected by both the charged condensate ρ and the source ρ_{src}, meaning that the last two terms in Eq. (5) cancel each other. Consider a time-harmonic source current $\mathbf{J}_{\mathrm{src}} = \mathbf{J}_0 e^{i\omega t}$ that, to first order in frequency, results in fluctuations in the gauge-invariant field $\boldsymbol{\mathcal{A}} = \boldsymbol{\mathcal{A}}_0 e^{i\omega t}$. According to Eq. (5), this, in turn, leads to a fluctuating condensate

$$\rho = \rho_0 + \delta\rho_0 e^{i\omega t}, \tag{A1}$$

where $\delta\rho_0 \ll \rho_0$. While the quadratic term $\partial_t \nabla |\boldsymbol{\mathcal{A}}|^2$ does not have a first-order contribution and can be ignored, the last term on the left-hand side of Eq. (4), which is related to the rate of change of the quantum pressure, needs careful consideration:

$$\begin{aligned}
&\frac{\mu_0\epsilon_0\hbar^2}{2mq}\frac{\partial}{\partial t}\nabla\left[\frac{\nabla^2(\sqrt{\rho})}{\sqrt{\rho}}\right] \\
&\quad= \frac{\mu_0\epsilon_0\hbar^2}{4mq}\nabla\left[\left(\frac{1}{\rho}\nabla^2 + \frac{|\nabla\rho|^2}{\rho^3} - \frac{\nabla^2\rho}{\rho^2} - \frac{\nabla\rho\cdot\nabla}{\rho}\right)\frac{\partial\rho}{\partial t}\right] \\
&\quad= \frac{\mu_0\epsilon_0\hbar^2}{4m^2}\nabla\nabla^2\nabla\cdot\boldsymbol{\mathcal{A}},
\end{aligned} \tag{A2}$$

where in the last line of Eq. (A2) we have used the ansatz (A1) for ρ with ρ_0 being a stepwise constant function, used Eq. (5) to replace the time derivative $\partial_t\rho$, and kept only the leading-order terms. For transverse excitations, the operation on $\boldsymbol{\mathcal{A}}$ in Eq. (A2) vanishes, resulting in the inhomogeneous source-field equation

$$\nabla\times\nabla\times\boldsymbol{\mathcal{A}}_0 + \left(\frac{1}{\lambda_L^2(\mathbf{r})} - n^2(\mathbf{r})k^2\right)\boldsymbol{\mathcal{A}}_0 = \mathbf{J}_0, \tag{A3}$$

where $\lambda_L(\mathbf{r}) = \sqrt{m/\mu_0 q^2 \rho_0(\mathbf{r})}$ is the London penetration depth, $n(\mathbf{r}) = \sqrt{\tilde{\epsilon}(\mathbf{r})}$, and $k = \mu_0\epsilon_0\omega^2$.

APPENDIX B: DERIVATION OF GREEN'S BOUNDARY INTEGRALS

In this appendix, we provide the derivations of the integral forms of the boundary fields that obey the scalar and vector Helmholtz equations as shown in Eqs. (16) and (18), respectively.

For a homogeneous domain Γ_i bounded by the boundary $\partial\Gamma_i$, the Green's function is the solution of the impulse response of the scalar Helmholtz operator and is defined by

$$\left[\nabla^2 + n_i^2 k^2\right] G(\mathbf{r}, \mathbf{r}', k) = \delta(\mathbf{r} - \mathbf{r}'), \tag{B1}$$

where $\delta(\mathbf{r} - \mathbf{r}')$ is a d-dimensional Dirac δ function. Multiplying Eq. (13) by $G(\mathbf{r}, \mathbf{r}', k)$ and Eq. (B1) by $\phi(\mathbf{r})$, and then applying Green's theorem, we obtain

$$\phi(\mathbf{r}') = \int_{\partial\Gamma_i}\left[\phi(\mathbf{r})\nabla G(\mathbf{r}, \mathbf{r}', k) - G(\mathbf{r}, \mathbf{r}', k)\nabla\phi(\mathbf{r})\right]\cdot\mathbf{ds}, \tag{B2}$$

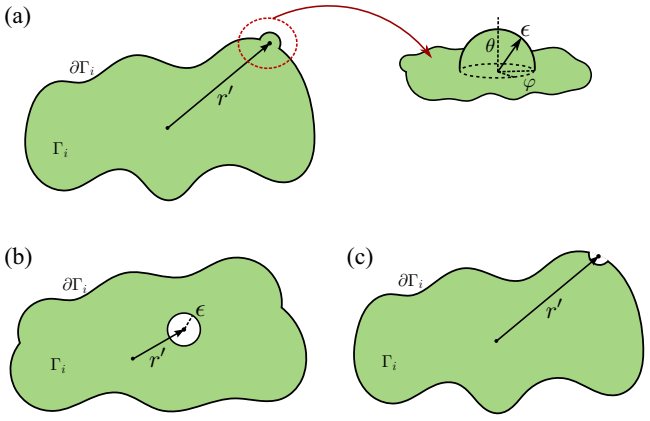

FIG. 12. Sketches showing how deformations are done to evaluate diverging integrals containing the Green's function. (a) Deformation on the boundary to include the boundary point. (b) Insertion of a hollow region internal to Γ_i surrounding the point of interest. (c) Deformation of the boundary to exclude the boundary point of interest.

for $\mathbf{r}'$ strictly inside the domain boundary $\partial\Gamma_i$. As we take the limit $\mathbf{r}' \to \partial\Gamma_i$, both $G(\mathbf{r}, \mathbf{r}', k)$ and its normal gradient diverge. However, we can show for the 3D case that Eq. (B2) is still integrable. A proof for two dimensions can be found in Ref. [76]. We first consider an infinitesimal half-spherical deformation C of the boundary at $\mathbf{r}'$ such that the surface now avoids and encloses the singular point inside the domain Γ_i as seen in Fig. 12(a). If radius of the deformation is ϵ, then at the limit $\epsilon \to 0$, the integral of the second term in Eq. (B2) over C vanishes,

$$\lim_{\epsilon\to 0}\int_C G(\mathbf{r}, \mathbf{r}', k)\nabla\phi(\mathbf{r})\cdot\mathbf{ds} = \lim_{\epsilon\to 0} -\frac{\partial\phi}{\partial n}\bigg|_{\mathbf{r}'}\frac{1}{4\pi}\left(\frac{1}{\epsilon} + in_i k + \ldots\right)2\pi\epsilon^2 = 0, \tag{B3}$$

while the integral of the first term over C gives

$$\lim_{\epsilon\to 0}\int_C \phi\frac{\partial G}{\partial n}ds = \lim_{\epsilon\to 0} -\phi(\mathbf{r}')\frac{e^{in_i k\epsilon}}{4\pi}\left(\frac{in_i k}{\epsilon} - \frac{1}{\epsilon^2}\right)2\pi\epsilon^2 = \frac{1}{2}\phi(\mathbf{r}'), \tag{B4}$$

where in the maneuvers above we have used the series expansion of the Green's function, which reads

$$G(\mathbf{r}, \mathbf{r}', k) = -\frac{e^{in_i k|\mathbf{r}-\mathbf{r}'|}}{4\pi|\mathbf{r}-\mathbf{r}'|} = -\left(\frac{1}{|\mathbf{r}-\mathbf{r}'|} + in_i k + \cdots\right). \tag{B5}$$

From the results in Eqs. (B3) and (B4) it follows that the integral in Eq. (B2) when $\mathbf{r}' \in \partial\Gamma_i$ evaluated over the entire boundary surface is indeed of the form shown in Eq. (16).

For the vector case, we start by introducing the vector analog of Green's identity

$$\int_{\Gamma_i}(\mathbf{u}\cdot\nabla\times\nabla\times\mathbf{v} - \mathbf{v}\cdot\nabla\times\nabla\times\mathbf{u})\,dV = \int_{\partial\Gamma_i}(\mathbf{v}\times\nabla\times\mathbf{u} - \mathbf{u}\times\nabla\times\mathbf{v})\cdot\mathbf{ds}, \tag{B6}$$

where $\mathbf{u}$ and $\mathbf{v}$ are vector fields. We now choose $\mathbf{v} = \boldsymbol{\mathcal{A}}(\mathbf{r})$, our field of interest, and $\mathbf{u} = \mathbf{G} \equiv G(\mathbf{r}, \mathbf{r}', k)\hat{\mathbf{v}}$, where $\hat{\mathbf{v}}$ is a unit vector that has a randomly selected, but constant, orientation. For a point $\mathbf{r}'$ outside Γ_i, Eq. (B6) reduces to

$$\begin{aligned}\int_{\Gamma_i}(\hat{\mathbf{v}}\cdot\nabla G)(\nabla\cdot\boldsymbol{\mathcal{A}})dV &= \int_{\partial\Gamma_i}\big\{(\hat{\mathbf{v}}\cdot\nabla G)(\boldsymbol{\mathcal{A}}\cdot\hat{\mathbf{n}}) + \boldsymbol{\mathcal{A}} \\ &\quad\times(\nabla G\times\hat{\mathbf{v}}) - \mathbf{G}\times\nabla\times\boldsymbol{\mathcal{A}}\big\}\cdot\mathbf{ds} \\ &= \int_{\partial\Gamma_i}\big\{(\hat{\mathbf{v}}\cdot\nabla G)(\boldsymbol{\mathcal{A}}\cdot\hat{\mathbf{n}}) + (\hat{\mathbf{v}}\cdot\boldsymbol{\mathcal{A}})(\nabla G\cdot\hat{\mathbf{n}}) \\ &\quad - (\hat{\mathbf{v}}\cdot\hat{\mathbf{n}})(\nabla G\cdot\boldsymbol{\mathcal{A}}) - \mathbf{G}\cdot\big[(\nabla\times\boldsymbol{\mathcal{A}})\times\hat{\mathbf{n}}\big]\big\}\,ds,\end{aligned} \tag{B7}$$

where $\hat{\mathbf{n}}$ is the unit normal vector on $\partial\Gamma_i$. Since $\hat{\mathbf{v}}$ is a common factor in all the terms, it can be dropped, and we arrive at

$$\int_{\Gamma_i}\nabla G(\nabla\cdot\boldsymbol{\mathcal{A}})dV = \int_{\partial\Gamma_i}\big\{\nabla G(\boldsymbol{\mathcal{A}}\cdot\hat{\mathbf{n}}) + \nabla G\times(\boldsymbol{\mathcal{A}}\times\hat{\mathbf{n}}) - G\big[(\nabla\times\boldsymbol{\mathcal{A}})\times\hat{\mathbf{n}}\big]\big\}\,ds. \tag{B8}$$

We are interested in, however, the evaluation of the field inside Γ_i. To proceed, consider when $\mathbf{r}'$ is inside the material region enclosed by $\partial\Gamma_i$ but there exists an infinitesimally small spherical hole S of radius ϵ centered at $\mathbf{r}'$. The boundary of Γ_i now consists of the original outer surface $\partial\Gamma_i$ and the boundary of the sphere, as seen in Fig. 12(b). At the limit $\epsilon \to 0$, each term in Eq. (B8) evaluated on the sphere gives

$$\lim_{\epsilon\to 0}\int_S G\big[(\nabla\times\boldsymbol{\mathcal{A}})\times\hat{\mathbf{n}}\big]ds = \lim_{\epsilon\to 0} -\frac{e^{in_j k\epsilon}}{4\pi\epsilon}\big[(\nabla\times\boldsymbol{\mathcal{A}})\times\hat{\mathbf{n}}\big]\Big|_{\mathbf{r}'}4\pi\epsilon^2 = 0, \tag{B9}$$

and also

$$\lim_{\epsilon\to 0}\int_S\big\{\nabla G(\boldsymbol{\mathcal{A}}\cdot\hat{\mathbf{n}}) + \nabla G\times(\boldsymbol{\mathcal{A}}\times\hat{\mathbf{n}})\big\}\,ds = \lim_{\epsilon\to 0}\int_S\left(\frac{1}{\epsilon} - in_i k\right)\frac{e^{in_i k\epsilon}}{4\pi\epsilon}\boldsymbol{\mathcal{A}}ds = \boldsymbol{\mathcal{A}}(\mathbf{r}'). \tag{B10}$$

Therefore, the integral form of the field at $\mathbf{r}'$ inside Γ_i is given by

$$\boldsymbol{\mathcal{A}}(\mathbf{r}') = \int_{\partial\Gamma_i} \left\{ G\left[(\nabla \times \boldsymbol{\mathcal{A}}) \times \hat{\mathbf{n}}\right] - \nabla G(\boldsymbol{\mathcal{A}} \cdot \hat{\mathbf{n}}) - \nabla G \times (\mathbf{A} \times \hat{\mathbf{n}}) \right\} + \int_{\Gamma_i} \nabla G(\nabla \cdot \boldsymbol{\mathcal{A}}) dV, \tag{B11}$$

where the volume term on the right-hand side is an improper integral. However, this term vanishes if the field is divergence-free, in which case the field anywhere strictly inside Γ_i is determined by the field on the boundary $\partial\Gamma_i$.

Finally, to find the integral form of the field on the boundary, at $\mathbf{r}' \in \partial\Gamma_i$, we consider a half-spherical deformation of $\partial\Gamma_i$ such that the boundary avoids $\mathbf{r}'$ and leaves it outside the enclosed domain Γ_i, as shown in Fig. 12(c). Note that this deformation is in the direction opposite that in the scalar case discussed earlier, where $\mathbf{r}'$ was included into Γ_i. By following a similar limiting procedure as laid out above for $\mathbf{r}'$ strictly inside Γ_i but now applied to a half-sphere, we arrive at the self-consistent integral form for the boundary field shown in Eq. (18).

APPENDIX C: COARSE-GRAINED OPEN BOUNDARY CONDITIONS USING VSH

In this appendix, we derive the boundary conditions for the angular components of the field $\boldsymbol{\mathcal{A}}(\mathbf{r})$ satisfying the vector Helmholtz equation. We also discuss the DEC implementation of such conditions on the tangential boundary edges.

The series expansion of the $\boldsymbol{\mathcal{A}}^{(1)}$ component is

$$\begin{aligned}\boldsymbol{\mathcal{A}}^{(1)}(r,\theta,\varphi) &= \sum_{l,m} \tilde{a}^1_{lm} \mathcal{A}^{(1)}_{lm} \Psi_{lm}(r,\theta,\varphi) \\ &= \tilde{a}_{lm} \frac{1}{2l(l+1)} \left[\frac{H_{l+1/2}(kr)}{r^{3/2}} + \frac{k}{\sqrt{r}} \left(H_{l-1/2}(kr) - H_{l+3/2}(kr) \right) \right] \Psi_{lm}(r,\theta,\varphi).\end{aligned}$$

The coefficients $a^1_{lm}(R)$ in the expansion of the field on the boundary surface are then given by

$$\begin{aligned} a^1_{lm}(R) &= \tilde{a}^1_{lm} \mathcal{A}^{(1)}_{lm}(R) \frac{1}{2l(l+1)} \left[\frac{H_{l+1/2}(kr)}{r^{3/2}} + \frac{k}{\sqrt{r}} \left(H_{l-1/2}(kr) - H_{l+3/2}(kr) \right) \right] \\ &= \frac{1}{l(l+1)} \int d\Omega \boldsymbol{\mathcal{A}}^{(1)} \cdot \Psi^*_{lm} \\ &= \frac{1}{l(l+1)} \sum_f \frac{\Delta A(f)}{R^2} \boldsymbol{\mathcal{A}}_t(f) \cdot \Psi^*_{lm}(f), \end{aligned} \tag{C1}$$

where $\boldsymbol{\mathcal{A}}_t$ is the component of $\boldsymbol{\mathcal{A}}(\mathbf{r})$ tangential to the boundary surface, and the sum is performed over all the triangular faces f on the boundary. In the last line of Eq. (C1) we have used the orthogonality between $\boldsymbol{\mathcal{A}}^{(1)}$ and Ψ^*_{lm} to switch to using $\boldsymbol{\mathcal{A}}_t$ instead of $\boldsymbol{\mathcal{A}}^{(1)}$ in the computation of $a^1_{lm}(R)$, since the former is more readily accessible during numerical implementation. The field $\boldsymbol{\mathcal{A}}^{(1)}$ can be decomposed into azimuthal and polar contributions, for each of which we derive the boundary condition. The radial derivative of the polar component of $\boldsymbol{\mathcal{A}}^{(1)}$ at the boundary is given by

$$\begin{aligned} &\frac{\mathcal{A}^{(1)}_\theta(R,\theta,\varphi) - \mathcal{A}^{(1)}_\theta(R-\Delta R,\theta,\varphi)}{\Delta R} \\ &= \sum_{l,m} \tilde{a}^{(1)}_{lm} \frac{1}{2l(l+1)} \left[\frac{H_{l+1/2}(kr)}{r^{1/2}} + k\sqrt{r} \left(H_{l-1/2}(kr) - H_{l+3/2}(kr) \right) \right]' \Big|_R (\nabla Y_{lm})_\theta, \end{aligned} \tag{C2}$$

from which the expression for $\mathcal{A}_\theta^{(1)}$ on the boundary surface can be extracted:

$$\mathcal{A}_\theta^{(1)}(R,\theta,\varphi) = \sum_{l,m} a_{lm}^{(1)}(R) \times \left(R + \Delta R \left\{ 1 + R \frac{\left[\frac{H_{l+1/2}(kr)}{r^{3/2}} + \frac{k}{\sqrt{r}} \left(H_{l-1/2}(kr) - H_{l+3/2}(kr) \right) \right]' \Big|_R}{\left[\frac{H_{l+1/2}(kR)}{R^{3/2}} + \frac{k}{\sqrt{R}} \left(H_{l-1/2}(kR) - H_{l+3/2}(kR) \right) \right]} \right\} \right) (\nabla Y_{lm})_\theta, \tag{C3}$$

where $(\nabla Y_{lm})_\theta$ is the polar component of ∇Y_{lm}, and $a_{lm}^1(R)$ is given as in Eq. (C1). The expression for the azimuthal component $\mathcal{A}_\varphi^{(1)}(R,\theta,\varphi)$ is similar, with replacement of θ by φ in the subscripts in Eq. (C3). Similarly to the steps for $\mathcal{A}^{(1)}$, the derivation of the BC for $\mathcal{A}^{(2)}$ starts with the expansion

$$\boldsymbol{\mathcal{A}}^{(2)} = \sum_{l.m} \tilde{a}_{lm}^{(2)} \frac{\pi}{2kR} H_{l+1/2}(kR) \boldsymbol{\Phi}_{l.m}(r,\theta,\varphi), \tag{C4}$$

from which the coefficients $a_{lm}^{(2)}$ can be computed:

$$\begin{aligned} a_{lm}^{(2)}(R) &= \tilde{a}_{lm}^{(2)} \frac{\pi}{2kR} H_{l+1/2}(kR) \\ &= \frac{1}{l(l+1)} \int d\Omega \boldsymbol{\mathcal{A}}^{(2)} \cdot \boldsymbol{\Phi}_{lm}^* \\ &= \frac{1}{l(l+1)} \sum_f \frac{\Delta A(f)}{R^2} \boldsymbol{\mathcal{A}}_t(f) \cdot \boldsymbol{\Phi}_{lm}^*(f). \end{aligned} \tag{C5}$$

We also write the boundary conditions for $\mathcal{A}_\theta^{(2)}$ and $\mathcal{A}_\varphi^{(2)}$ separately using their discrete form of the radial derivative at the boundary. This leads to

$$\begin{aligned} \mathcal{A}_\theta^{(2)}(R,\theta,\varphi) = \sum_{l,m} a_{lm}^{(2)}(R) \Bigg\{ R + \frac{\Delta R}{2} \\ \times \left[1 + kR \frac{H_{l-1/2}(kR) - H_{l+3/2}(kR)}{H_{l+1/2}(kR)} \right] \Bigg\} \\ \times (\hat{\mathbf{r}} \times \nabla Y_{lm})_\theta, \end{aligned} \tag{C6}$$

and by replacing θ with φ in the subscripts, we obtain the expression for $\mathcal{A}_\varphi^{(2)}(R,\theta,\varphi)$.

The boundary conditions given in Eqs. (C3) and (C6) are for vector individual components, which are scalars lying on vertices of the primal computational mesh. We would like to translate these BCs to fields lying on the edges that lie on the boundary surface. First of all, the practical computation of the expansion coefficients in Eqs. (C1) and (C5) requires knowledge of the tangential field $\boldsymbol{\mathcal{A}}_t$ defined on the centers of the triangular faces f that discretize the boundary surface. In DEC, however, vectors are replaced by their projections onto the discrete edges, which are quantities that we have access to. Therefore, at each triangular face, given the edge fields that are on the three sides of the triangle, we need to determine the value of the vector $\boldsymbol{\mathcal{A}}_t$ at the circumcenter f [†]. This mapping from primal edge field to dual vector field is done through a sharp (#) operator, whose formal definition is given in Ref. [80]. Now given that the coefficient expansions are obtained, for every vertex on the boundary, the polar (azimuthal) component of $\mathcal{A}_t$ is the sum of projections from $\mathcal{A}^{(1)}$ and $\mathcal{A}^{(2)}$:

$$\mathcal{A}_{\theta(\varphi)}(R,\theta,\varphi) = \mathcal{A}_{\theta(\varphi)}^{(1)}(R,\theta,\varphi) + \mathcal{A}_{\theta(\varphi)}^{(2)}(R,\theta,\varphi). \tag{C7}$$

For an edge $e[v_1, v_2]$ lying on the boundary, where v_1 and v_2 are the starting and ending vertices of the edge, the edge field is given by

$$\boldsymbol{\Phi}(e[v_1,v_2]) = \frac{[\boldsymbol{\mathcal{A}}_t(v_1) + \boldsymbol{\mathcal{A}}_t(v_2)]}{2} \cdot (\mathbf{v}_2 - \mathbf{v}_1), \tag{C8}$$

where $\mathbf{v}_1$ and $\mathbf{v}_2$ are the locations of the vertices v_1 and v_2, respectively, with the components of $\boldsymbol{\mathcal{A}}_t$ on the boundary given in Eq. (C7). Equation (C8) is the boundary condition to be imposed on the edges lying tangentially to the boundary surface.

APPENDIX D: SEPARABILITY OF THE HELMHOLTZ EQUATION IN ELLIPSOIDAL COORDINATES

The ellipsoidal coordinate system is based on the equation

$$\frac{x^2}{\xi_i^2 - a^2} + \frac{y^2}{\xi^2 - b^2} + \frac{z^2}{\xi^2 - c^2} = 1, \tag{D1}$$

where $a \geq b \geq c$ and $i = 1, 2, 3$ such that

$$\xi_1 > a > \xi_2 > b > \xi_3 > c. \tag{D2}$$

Equation (D1) represents three families of confocal quadric surfaces sharing the same foci. In the discussion here, to simplify the algebraic manipulations we consider

the case where $c = 0$. The relationships between the ellipsoidal coordinates (ξ_1, ξ_2, ξ_3) and the Cartesian coordinates are given by

$$x = \sqrt{\frac{(\xi_1^2 - a^2)(\xi_2^2 - a^2)(\xi_3^2 - a^2)}{a^2(a^2 - b^2)}},$$
$$y = \sqrt{\frac{(\xi_1^2 - b^2)(\xi_2^2 - b^2)(\xi_3^2 - b^2)}{b^2(b^2 - a^2)}}, \tag{D3}$$
$$z = \frac{\xi_1\xi_2\xi_3}{ab},$$

with the scale factors being

$$h_1 = \sqrt{\frac{(\xi_1^2 - \xi_2^2)(\xi_1^2 - \xi_3^2)}{(\xi_1^2 - a^2)(\xi_1^2 - b^2)}},$$
$$h_2 = \sqrt{\frac{(\xi_2^2 - \xi_1^2)(\xi_2^2 - \xi_3^2)}{(\xi_2^2 - a^2)(\xi_2^2 - b^2)}}. \tag{D4}$$

The Helmholtz equation [Eq. (13)] is separable in 11 three-dimensional coordinate systems, with the ellipsoidal coordinates being the most general of them and the remaining ten—including the spherical coordinates used in the main text—being derived from them through limiting processes [81]. The separability in ellipsoidal coordinates can be shown by one using the ansatz

$$\phi(\xi_1, \xi_2, \xi_3) = \psi_1(\xi_1)\psi_2(\xi_2)\psi_3(\xi_3) \tag{D5}$$

for the field in Eq. (13), resulting in separated ordinary differential equations of the form

$$4\sqrt{f(\kappa_i)}\frac{d}{d\kappa_i}\left(\sqrt{f(\kappa_i)}\frac{d\psi_i}{d\kappa_i} + (\lambda_1 + \lambda_2\kappa_i + k^2\kappa_i^2)\right)\psi_i = 0, \tag{D6}$$

where $f(\kappa_i) = \sqrt{(\kappa_i - a^2)(\kappa_i^2 - b^2)\kappa_i}$, with $\kappa_i = \xi^2$. On performing a change of variables

$$\kappa_i = b^2 sn^2\left(\alpha, \frac{b^2}{a^2}\right), \tag{D7}$$

where $sn(u, m)$ is a Jacobi elliptic function, we can write

$$f(\kappa_i) = b^4a^2 sn^2\left(\alpha, \frac{b^2}{a^2}\right) dn^2\left(\alpha, \frac{b^2}{a^2}\right) cn^2\left(\alpha, \frac{b^2}{a^2}\right), \tag{D8}$$

with $dn(u, m)$ and $cn(u, m)$ also Jacobi elliptic functions. Equation (D6) can then be written in terms of the new variable as

$$\frac{d^2\psi_i}{d\alpha^2} + \left[\frac{\lambda_1}{a^2} + \frac{\lambda_2}{a^2}sn^2\left(\alpha, \frac{b^2}{a^2}\right) + \frac{k^2}{a^2}sn^4\left(\alpha, \frac{b^2}{a^2}\right)\right]\psi_i = 0. \tag{D9}$$

Equation (D9) is the ellipsoidal wave equation, whose solutions are known as ellipsoidal wave functions. With the Helmholtz equation being separable in ellipsoidal coordinates with known solutions, the generalization to this coordinate system of our spherical harmonics method for open systems is therefore straightforward.

[1] A. A. Houck, H. E. Türeci, and J. Koch, On-chip quantum simulation with superconducting circuits, Nat. Phys. **8**, 292 (2012).

[2] I. Carusotto, A. A. Houck, A. J. Kollár, P. Roushan, D. I. Schuster, and J. Simon, Photonic materials in circuit quantum electrodynamics, Nat. Phys. **16**, 268 (2020).

[3] M. Hatridge, R. Vijay, D. Slichter, J. Clarke, and I. Siddiqi, Dispersive magnetometry with a quantum limited squid parametric amplifier, Phys. Rev. B **83**, 134501 (2011).

[4] C. Macklin, K. O'brien, D. Hover, M. Schwartz, V. Bolkhovsky, X. Zhang, W. Oliver, and I. Siddiqi, A near–quantum-limited Josephson traveling-wave parametric amplifier, Science **350**, 307 (2015).

[5] A. Blais, R.-S. Huang, A. Wallraff, S. M. Girvin, and R. J. Schoelkopf, Cavity quantum electrodynamics for superconducting electrical circuits: An architecture for quantum computation, Phys. Rev. A **69**, 062320 (2004).

[6] M. H. Devoret and R. J. Schoelkopf, Superconducting circuits for quantum information: An outlook, Science **339**, 1169 (2013).

[7] R. P. Feynman, R. B. Leighton, and M. Sands, in *The Feynman Lectures on Physics* (Addison–Wesley, New York, 1965), Vol. III, Chap. 21.

[8] P. Ao, D. J. Thouless, and X.-M. Zhu, Nonlinear Schrödinger equation for superconductors, Mod. Phys. Lett. B **9**, 755 (1995).

[9] I. J. Aitchison, P. Ao, D. J. Thouless, and X.-M. Zhu, Effective Lagrangians for BCS superconductors at $T = 0$, Phys. Rev. B **51**, 6531 (1995).

[10] D. N. Pham, W. Fan, M. G. Scheer, and H. E. Türeci, Flux-based three-dimensional electrodynamic modeling approach to superconducting circuits and materials, Phys. Rev. A **107**, 053704 (2023).

[11] M. Greiter, F. Wilczek, and E. Witten, Hydrodynamic relations in superconductivity, Mod. Phys. Lett. B **3**, 903 (1989).

[12] M. P. A. Fisher, G. Grinstein, and S. M. Girvin, Presence of quantum diffusion in two dimensions: Universal resistance at the superconductor-insulator transition, Phys. Rev. Lett. **64**, 587 (1990).

[13] L. Salasnich, Hydrodynamics of Bose and Fermi superfluids at zero temperature: The superfluid nonlinear Schrödinger equation, Laser Phys. **19**, 642 (2009).

[14] A. Blais, A. L. Grimsmo, S. M. Girvin, and A. Wallraff, Circuit quantum electrodynamics, Rev. Mod. Phys. **93**, 025005 (2021).

[15] S. E. Nigg, H. Paik, B. Vlastakis, G. Kirchmair, S. Shankar, L. Frunzio, M. H. Devoret, R. J. Schoelkopf, and S. M. Girvin, Black-box superconducting circuit quantization, Phys. Revs. Lett. **108**, 240502 (2012).

[16] F. Solgun and D. P. DiVincenzo, Multiport impedance quantization, Ann. Phys. **361**, 605 (2015).
[17] W. C. Smith, A. Kou, U. Vool, I. M. Pop, L. Frunzio, R. J. Schoelkopf, and M. H. Devoret, Quantization of inductively shunted superconducting circuits, Phys. Rev. B **94**, 144507 (2016).
[18] M. Malekakhlagh and H. E. Türeci, Origin and implications of an A^2-like contribution in the quantization of circuit-QED systems, Phys. Rev. A **93**, 012120 (2016).
[19] A. Parra-Rodriguez, I. Egusquiza, D. DiVincenzo, and E. Solano, Canonical circuit quantization with linear nonreciprocal devices, Phys. Rev. B **99**, 014514 (2019).
[20] Z. K. Minev, Z. Leghtas, S. O. Mundhada, L. Christakis, I. M. Pop, and M. H. Devoret, Energy-participation quantization of Josephson circuits, npj Quantum Inf. **7**, 131 (2021).
[21] The time-coarse graining toolbox, https://github.com/leonbello/QuantumGraining.jl.
[22] A. Osborne and A. Lucas, Flux-charge symmetric theory of superconducting circuits, Phys. Rev. B **109**, 174524 (2024).
[23] G. Khan and T. E. Roth, in *2024 United States National Committee of URSI National Radio Science Meeting* (USNC-URSI NRSM, Boulder, CO, USA, 2024), pp. 196–196.
[24] A. Parra-Rodriguez and I. Egusquiza, Geometrical description and Faddeev-Jackiw quantization of electrical networks, Quantum **8**, 1466 (2024).
[25] A. Houck, J. Schreier, B. Johnson, J. Chow, J. Koch, J. Gambetta, D. Schuster, L. Frunzio, M. Devoret, S. Girvin *et al.*, Controlling the spontaneous emission of a superconducting transmon qubit, Phys. Rev. Lett. **101**, 080502 (2008).
[26] M. D. Reed, B. R. Johnson, A. A. Houck, L. DiCarlo, J. M. Chow, D. I. Schuster, L. Frunzio, and R. J. Schoelkopf, Fast reset and suppressing spontaneous emission of a superconducting qubit, Appl. Phys. Lett. **96**, 203110 (2010).
[27] E. Jeffrey, D. Sank, J. Y. Mutus, T. C. White, J. Kelly, R. Barends, Y. Chen, Z. Chen, B. Chiaro, A. Dunsworth, A. Megrant, P. J. J. O'Malley, C. Neill, P. Roushan, A. Vainsencher, J. Wenner, A. N. Cleland, and J. M. Martinis, Fast accurate state measurement with superconducting qubits, Phys. Rev. Lett. **112**, 190504 (2014).
[28] N. T. Bronn, Y. Liu, J. B. Hertzberg, A. D. Córcoles, A. A. Houck, J. M. Gambetta, and J. M. Chow, Broadband filters for abatement of spontaneous emission in circuit quantum electrodynamics, Appl. Phys. Lett. **107**, 172601 (2015).
[29] M. Boissonneault, J. M. Gambetta, and A. Blais, Dispersive regime of circuit QED: Photon-dependent qubit dephasing and relaxation rates, Phys. Rev. A **79**, 013819 (2009).
[30] D. H. Slichter, R. Vijay, S. J. Weber, S. Boutin, M. Boissonneault, J. M. Gambetta, A. Blais, and I. Siddiqi, Measurement-induced qubit state mixing in circuit QED from up-converted dephasing noise, Phys. Rev. Lett. **109**, 153601 (2012).
[31] S. Mundhada, S. Shankar, A. Narla, E. Zalys-Geller, S. Girvin, and M. Devoret, Dependence of transmon qubit relaxation rate on readout drive power, APS March Meeting **V48** (2016).
[32] Z. Minev, S. Mundhada, S. Shankar, P. Reinhold, R. Gutiérrez-Jáuregui, R. Schoelkopf, M. Mirrahimi, H. Carmichael, and M. Devoret, To catch and reverse a quantum jump mid-flight, Nature **570**, 200 (2019).
[33] A. Petrescu, M. Malekakhlagh, and H. E. Türeci, Lifetime renormalization of driven weakly anharmonic superconducting qubits. II. The readout problem, Phys. Rev. B **101**, 134510 (2020).
[34] R. Hanai, A. McDonald, and A. Clerk, Intrinsic mechanisms for drive-dependent Purcell decay in superconducting quantum circuits, Phys. Rev. Res. **3**, 043228 (2021).
[35] D. Gusenkova, M. Spiecker, R. Gebauer, M. Willsch, D. Willsch, F. Valenti, N. Karcher, L. Grünhaupt, I. Takmakov, P. Winkel, D. Rieger, A. V. Ustinov, N. Roch, W. Wernsdorfer, K. Michielsen, O. Sander, and I. M. Pop, Quantum nondemolition dispersive readout of a superconducting artificial atom using large photon numbers, Phys. Rev. Appl. **15**, 064030 (2021).
[36] R. Shillito, A. Petrescu, J. Cohen, J. Beall, M. Hauru, M. Ganahl, A. G. Lewis, G. Vidal, and A. Blais, Dynamics of transmon ionization, Phys. Rev. Appl. **18**, 034031 (2022).
[37] J. Cohen, A. Petrescu, R. Shillito, and A. Blais, Reminiscence of classical chaos in driven transmons, PRX Quantum **4**, 020312 (2023).
[38] A. Caldeira and A. Leggett, Quantum tunnelling in a dissipative system, Ann. Phys. **149**, 374 (1983).
[39] S. Filipp, M. Göppl, J. M. Fink, M. Baur, R. Bianchetti, L. Steffen, and A. Wallraff, Multimode mediated qubit-qubit coupling and dark-state symmetries in circuit quantum electrodynamics, Phys. Rev. A **83**, 063827 (2011).
[40] C. Bergenfeldt and P. Samuelsson, Microwave quantum optics and electron transport through a metallic dot strongly coupled to a transmission line cavity, Phys. Rev. B **85**, 045446 (2012).
[41] M. Bamba and T. Ogawa, Recipe for the Hamiltonian of system-environment coupling applicable to the ultrastrong-light-matter-interaction regime, Phys. Rev. A **89**, 023817 (2014).
[42] M. F. Gely, A. Parra-Rodriguez, D. Bothner, Y. M. Blanter, S. J. Bosman, E. Solano, and G. A. Steele, Convergence of the multimode quantum Rabi model of circuit quantum electrodynamics, Phys. Rev. B **95**, 245115 (2017).
[43] M. Malekakhlagh, A. Petrescu, and H. E. Türeci, Cutoff-free circuit quantum electrodynamics, Phys. Rev. Lett. **119**, 073601 (2017).
[44] A. Parra-Rodriguez, E. Rico, E. Solano, and I. Egusquiza, Quantum networks in divergence-free circuit QED, Quantum Sci. Technol. **3**, 024012 (2018).
[45] T. Shitara, M. Bamba, F. Yoshihara, T. Fuse, S. Ashhab, K. Semba, and K. Koshino, Nonclassicality of open circuit QED systems in the deep-strong coupling regime, New J. Phys. **23**, 103009 (2021).
[46] J. Bourassa, F. Beaudoin, J. M. Gambetta, and A. Blais, Josephson-junction-embedded transmission-line resonators: From Kerr medium to in-line transmon, Phys. Rev. A **86**, 013814 (2012).
[47] F. Yoshihara, Y. Nakamura, F. Yan, S. Gustavsson, J. Bylander, W. D. Oliver, and J.-S. Tsai, Flux qubit noise spectroscopy using Rabi oscillations under strong driving conditions, Phys. Rev. B **89**, 020503 (2014).

[48] P. Kumar, S. Sendelbach, M. Beck, J. Freeland, Z. Wang, H. Wang, C. Y. Clare, R. Wu, D. Pappas, and R. McDermott, Origin and reduction of $1/f$ magnetic flux noise in superconducting devices, Phys. Rev. Appl. **6**, 041001 (2016).

[49] C. D. Wilen, S. Abdullah, N. Kurinsky, C. Stanford, L. Cardani, G. d'Imperio, C. Tomei, L. Faoro, L. Ioffe, C. Liu *et al.*, Correlated charge noise and relaxation errors in superconducting qubits, Nature **594**, 369 (2021).

[50] I. M. Pop, K. Geerlings, G. Catelani, R. J. Schoelkopf, L. I. Glazman, and M. H. Devoret, Coherent suppression of electromagnetic dissipation due to superconducting quasiparticles, Nature **508**, 369 (2014).

[51] N. Frattini, V. Sivak, A. Lingenfelter, S. Shankar, and M. Devoret, Optimizing the nonlinearity and dissipation of a snail parametric amplifier for dynamic range, Phys. Rev. Appl. **10**, 054020 (2018).

[52] J. Wenner, M. Neeley, R. C. Bialczak, M. Lenander, E. Lucero, A. D. O'Connell, D. Sank, H. Wang, M. Weides, A. N. Cleland, and J. M. Martinis, Wirebond crosstalk and cavity modes in large chip mounts for superconducting qubits, Supercond. Sci. Technol. **24**, 065001 (2011).

[53] S. Huang, B. Lienhard, G. Calusine, A. Vepsäläinen, J. Braumüller, D. K. Kim, A. J. Melville, B. M. Niedzielski, J. L. Yoder, B. Kannan *et al.*, Microwave package design for superconducting quantum processors, PRX Quantum **2**, 020306 (2021).

[54] J.-P. Berenger, A perfectly matched layer for the absorption of electromagnetic waves, J. Comput. Phys. **114**, 185 (1994).

[55] J.-P. Berenger, Three-dimensional perfectly matched layer for the absorption of electromagnetic waves, J. Comput. Phys. **127**, 363 (1996).

[56] R. Clayton and B. Engquist, Absorbing boundary conditions for acoustic and elastic wave equations, Bull. Seismol. Soc. Am. **67**, 1529 (1977).

[57] R. L. Higdon, Numerical absorbing boundary conditions for the wave equation, Math. Comput. **49**, 65 (1987).

[58] M. Gell-Mann and F. E. Low, Quantum electrodynamics at small distances, Phys. Rev. **95**, 1300 (1954).

[59] B. Qi, L. Zhang, and L. Ge, Defect states emerging from a non-Hermitian flatband of photonic zero modes, Phys. Rev. Lett. **120**, 093901 (2018).

[60] R. El-Ganainy, K. G. Makris, M. Khajavikhan, Z. H. Musslimani, S. Rotter, and D. N. Christodoulides, Non-Hermitian physics and Pt symmetry, Nat. Phys. **14**, 11 (2018).

[61] C. Gigli, T. Wu, G. Marino, A. Borne, G. Leo, and P. Lalanne, Quasinormal-mode non-Hermitian modeling and design in nonlinear nano-optics, ACS Photonics **7**, 1197 (2020).

[62] K. Sinha, S. A. Khan, E. Cüce, and H. E. Türeci, Radiative properties of an artificial atom coupled to a Josephson-junction array, Phys. Rev. A **106**, 033714 (2022).

[63] E. M. Purcell, H. C. Torrey, and R. V. Pound, Resonance absorption by nuclear magnetic moments in a solid, Phys. Rev. **69**, 37 (1946).

[64] M. Malekakhlagh, A. Petrescu, and H. E. Türeci, Non-Markovian dynamics of a superconducting qubit in an open multimode resonator, Phys. Rev. A **94**, 063848 (2016).

[65] S. J. Bosman, M. F. Gely, V. Singh, A. Bruno, D. Bothner, and G. A. Steele, Multi-mode ultra-strong coupling in circuit quantum electrodynamics, npj Quantum Inf. **3**, 46 (2017).

[66] J. Puertas Martínez, S. Léger, N. Gheeraert, R. Dassonneville, L. Planat, F. Foroughi, Y. Krupko, O. Buisson, C. Naud, W. Hasch-Guichard *et al.*, A tunable Josephson platform to explore many-body quantum optics in circuit-QED, npj Quantum Inf. **5**, 19 (2019).

[67] T. E. Roth and W. C. Chew, Macroscopic circuit quantum electrodynamics: A new look toward developing full-wave numerical models, IEEE J. Multiscale Multiphys. Comput. Tech. **6**, 109 (2021).

[68] W. C. Chew, A. Y. Liu, C. Salazar-Lazaro, and W. E. Sha, Quantum electromagnetics: A new look—Part II, IEEE J. Multiscale Multiphys. Comput. Tech. **1**, 85 (2016).

[69] F. Solgun, D. W. Abraham, and D. P. DiVincenzo, Blackbox quantization of superconducting circuits using exact impedance synthesis, Phys. Rev. B **90**, 134504 (2014).

[70] H. E. Türeci, L. Ge, S. Rotter, and A. D. Stone, Strong interactions in multimode random lasers, Science **320**, 643 (2008).

[71] J. Wiersig, Boundary element method for resonances in dielectric microcavities, J. Opt. A: Pure Appl. Opt. **5**, 53 (2002).

[72] DEC-QED toolbox, https://github.com/dnpham23/DEC-QED.

[73] F. London and H. London, The electromagnetic equations of the supraconductor, Proc. R. Soc. Lond. Ser. A **149**, 71 (1935).

[74] G. B. Shaw, Degeneracy in the particle-in-a-box problem, J. Phys. A: Math. Nucl. Gen. **7**, 1537 (1974).

[75] B. D. Josephson, Supercurrents through barriers, Adv. Phys. **14**, 419 (1965).

[76] I. Kosztin and K. Schulten, Boundary integral method for stationary states of two-dimensional quantum systems, Int. J. Mod. Phys. C **8**, 293 (1997).

[77] D. N. Pham, S. Bharadwaj, S. Rodriguez, L. Rodriguez, and L. R. Ram-Mohan, High-accuracy calculation of singular electromagnetic fields in regions with re-entrant peripheries, J. Appl. Phys. **134**, 153102 (2023).

[78] A. Bäcker, in *The Mathematical Aspects of Quantum Maps*, edited by M. D. Esposti and S. Graffi (Springer, Berlin, Heidelberg, 2003), pp. 91–144.

[79] R. G. Barrera, G. Estevez, and J. Giraldo, Vector spherical harmonics and their application to magnetostatics, Eur. J. Phys. **6**, 287 (1985).

[80] A. N. Hirani, Discrete exterior calculus, Ph.D. thesis, California Institute of Technology, 2003.

[81] P. M. Morse and H. Feshbach, Methods of theoretical physics, Am. J. Phys. **22**, 410 (1954).